Universidad de Concepción
Dirección de Postgrado
Facultad de Ingeniería - Programa de Doctorado en Ciencias de la Ingeniería

MULTIDIMENTIONAL ANALYSIS FOR HYPERSPECTRAL IMAGING SYSTEMS: A TIME, SPACE AND WAVELENGTH APPROACH

PABLO FRANCISCO MEZA NARVAEZ
CONCEPCIÓN-CHILE
2014

Profesor Guía: Sergio Torres Inostroza
Dpto. de Ingeniería Eléctrica, Facultad de Ingeniería
Universidad de Concepción

Universidad de Concepción
Facultad de Ingeniería
Departamento de Ingeniería Eléctrica

MULTIDIMENSIONAL ANALYSIS FOR HYPERSPECTRAL IMAGING SYSTEMS: A TIME, SPACE AND WAVELENGTH APPROACH

Pablo Meza Narváez

Becario CONICYT 2009-2013

Supervisor: PhD. Sergio Torres Inostroza

Informe de Tesis
presentado a la Dirección de Postgrado
para optar al grado académico de

Doctor en Ciencias de la Ingeniería con mención Ingeniería Eléctrica

Enero 2014

The thesis of Pablo Meza Narváez was reviewed and approved by the following:

Sergio Torres Inostroza
PhD. in Engineering
Thesis Advisor, Chair of Committee

Jorge Pezoa Núñez
PhD. in Electrical Engineering
Reviewer

Daniel Sbárbaro Hofer
Ph.D. in Electrical Engineering
Reviewer

Carlos Saavedra Rubilar
PhD. in Physics
External Reviewer

Abstract

In this thesis, a novel pixel wise, affine image-degradation model for push-broom hyperspectral cameras (PBHCs) is proposed by considering an optoelectronic approach, and thereby generating an accurate mathematical representation of the hyperspectral acquisition process. The image-degradation model is linear and the parameters associated to the striping noise (SN) are assumed to be spatially uncorrelated, spectrally independent, and decoupled from camera's spectral response. The applicability of these assumptions was verified by an experimental characterization of the hyperspectral cameras in our disposal. Further, the spatial, spectral, and temporal information are assumed to be highly redundant due to the high spectral resolution and the fast temporal scanning of modern PBHCs. In this manner, and based on the proposed observation model, two novel multidimensional striping noise compensation (SNC) algorithms for PBHCs have been developed, the multidimensional neural network (NN) and moment matching (MM) algorithms. The algorithms simultaneously exploit the spatial and temporal information contained in a target scene as well as the spectral information contained at adjacent spectral images. The ability of the algorithms to estimate and compensate for the SN parameters, subject to the restrictions of the input radiation, was demonstrated mathematically. An additional algorithm has been included to relax the assumption of spectral redundancy, reducing the loss of spectral resolution in the hypercube. The applicability of the multidimensional SNC algorithms was successfully tested on real hyperspectral data acquired using a laboratory prototype, achieving compensated images remarkably good compared to their unidimensional versions. The experimental setup, based on both Photonfocus Hurricane and Xeva Xenics hyperspectral cameras, has been implemented to acquire data in the range of 400-1000 [nm] and 900-1700 [nm], respectively. It is worth mentioning that both cameras present distinctive noise patterns in terms of spectral structure. Further, a mobile platform was used to simulate and synchronize the scanning procedure of the cameras and a uniform tungsten lamp is installed to ensure an equal spectral

radiance between the different bands for calibration purposes. In addition, raw data recollected from the Earth-observing CHRIS/PROBA CCD sensor was tested.

Resumen

En esta tesis, se propone un novedoso modelo de degradación afín de imágenes para cámaras hiperespectrales de barrido (PBHCs), siguiendo un enfoque optoelectrónico y generando una representación matemática precisa del proceso de adquisición hiperespectral. El modelo de degradación de imagen es lineal y los parámetros asociados al ruido de franjas (SN) son asumidos espacialmente correlacionados, espectralmente independientes y desvinculados de la respuesta espectral de la cámara. La aplicabilidad de estos supuestos se verificó mediante una caracterización experimental de las cámaras hiperespectrales a nuestra disposición. Además, se asume que la información espacial, espectral, y temporal son altamente redundante debido a la alta resolución espectral y al rápido barrido temporal de las PBHCs modernas. De esta manera, y con base en el modelo de observación propuesto, se han desarrollado dos nuevos algoritmos multidimensionales de compensación de ruido de franjas (SNC) para PBHCs, los algoritmos multidimensionales de redes neuronales (NN) y de ajuste de momentos (MM). Los algoritmos explotan simultáneamente la información espacial y temporal contenida en una escena objetivo, así como la información espectral contenida en las imágenes espectrales adyacentes. La habilidad de los algoritmos de estimar y compensar los parámetros de SN, sujetos a las restricciones de la radiación de entrada, fue demostrada matemáticamente. Un algoritmo adicional ha sido incluido para relajar el supuesto de redundancia espectral, reduciendo la perdida de resolución espectral en el hipercubo. La aplicabilidad de los algoritmos SNC multidimensionales fue probada con éxito en datos hiperespectrales reales adquiridos usando un prototipo de laboratorio, logrando comparativamente mejores imágenes compensadas que sus versiones unidimensionales. Se ha implementado una configuración experimental, basada en las cámaras hiperespectrales Photonfocus Hurricane y Xeva Xenics, para adquirir datos en el rango de 400-1000 [nm] y 900-1700 [nm], respectivamente. Vale la pena mencionar que ambas cámaras presentan patrones distintivos de ruido en términos de estructura espectral. Además, se utilizó una plataforma móvil para simular y sin-

cronizar el procedimiento de barrido de las cámaras y, para fines de calibración, una lámpara de tungsteno uniforme fue instalada para asegurar una radiancia espectral igual entre las diferentes bandas. Además, para probar los algoritmos, se utilizaron los datos crudos recolectados desde el sensor CCD Earth-observing CHRIS/PROBA.

Table of Contents

List of Figures

List of Tables

List of Abbreviations

APS	active-pixel sensor
BF	bilateral filter
FPA	focal plane array
FWHM	full width at half maximum
IF	improvement factor
LMS	least mean square
MM	moment matching
NIR	near infrared
NU	non-uniformity
NUC	non-uniformity correction
NN	neural network
NR	noise reduction index
PBHC	push-broom hyperspectral camera
PPS	passive-pixel sensor
QTH	quartz tungsten halogen
RMSE	root mean squared error
SN	striping noise
SNC	striping noise compensation
SNR	signal-to-noise ratio
TFT	thin film transistor
VIS	visible
WBHC	whisk-broom hyperspectral camera

Acknowledgments

I would like to thank the Comisión Nacional de Ciencia y Tecnología (CONICYT), Chile, which funded my Ph.D studies from 2009 to 2013. Also, to the Center for Optics and Photonics for their technological support, which without this thesis would have been difficult to complete.

I would like to express my sincere gratitude to my advisor Professor Sergio Torres for his constant support of my studies and research, and for his patience, motivation, and vast knowledge. Also, I would like to thank Professor Jorge Pezoa for his extremely useful math lessons and guidance that helped me during the research and writing of this thesis. Further, I have to mention Professor Cesar San Martin, who guided me in this career path many years ago. To Sebastian and Esteban, who were the first to greet me in the lab. I will always remember the stimulating discussions and working together against aggressive deadlines. Your lessons are something that will accompany me for the rest of my professional career.

I am indebted to my many lab partners for providing a stimulating and fun environment. I am especially grateful to Francisca, Pablo, Miguel, Felipe, Carlos, Octavio, Elena, Philippe, Francisco, and Hector. I must also acknowledge Don Exequiel Campillo for his technical assistance throughout my graduate program. Furthermore, I would like to thank my friends in the Optical Tweezers and Microscopy Laboratory, particularly J.P. Staforelli and M.J. Gallardo, for our extended discussions and exchanges of knowledge.

Of course, thanks to my parents for giving birth to me in the first place and for their unconditional support throughout my life. Especially, I would like to give my special thanks to my dear wife Malú, whose patient love and support enabled me to complete this work. Without you by my side none of this would have been possible, I love you and the family we are building together more than anything in this world.

Dedication

To Malú and Renata...

Chapter 1

Introduction

In this chapter, a general overview of hyperspectral imaging systems is presented, from the optoelectronic acquisition mechanism to the signal modeling and the estimation schemes for the parameters model. Next, a general vision of the hyperspectral system, knowledge that becomes necessary for finding comprehensive solutions for problems where the available information is restricted, is obtained. We define our hypothesis and the objectives required to prove it, and finally, the organization of this thesis is depicted.

1.1 Hyperspectral Imaging: An Overview

A push-broom hyperspectral camera (PBHC) is an imaging system which collects, for each spatial location being imaged, a set of hundreds of high spectral resolution images that jointly form the spectrum of a target scene. This set of hyperspectral images is termed as "the hypercube" [1]. PBHCs have become popular in all sorts of scientific and industrial applications due to the high spectral resolution of the images in the hypercube. Examples of such applications are remote sensing [1], food science and engineering [2], and chemical imaging [3].

A PBHC can be described, in brief, as an optoelectronic system composed of four sub-systems: the optics, the spectrograph, the sensor, and the readout electronics [1]. The front-end sub-system is the optics, which is formed by the lens, whose purpose is to focus the incoming radiance onto the next sub-system: the spectrograph. The spectrograph is, typically, a slit-based diffraction grating that limits the area of ob-

servation to a single line while simultaneously forming a spectrum of the line being imaged. The third sub-system is the sensor, which is typically a two-dimensional focal plane array (FPA) that collects the spatio-spectral information of the line image by converting the photon energy into an electric charge. For PBHCs, unlike broadband imagers, the spatial information is mapped onto one FPA dimension, while the spectral information is mapped onto the FPA's second dimension. Therefore, a target scene must be scanned one line at a time by moving the camera along a trajectory orthogonal to the dimension used to encode the spectral information. Finally, the readout electronics is the sub-system retrieving sensor's electric charge, which is converted into a voltage signal that is amplified, and ultimately, converted to digital counts at each pixel.

As any practical device, a PBHC is affected by different noise sources, which may arise at every part of the system. For instance, at the optics sub-system, blurring occurs due to lens imperfections or lack of focusing [4]. At the spectrograph, variations in the slit's width introduce non-uniformity (NU) in the number of photons collected per spectral band [5]. At the sensor sub-system, manufacturing imperfections introduce further variations in the number of photons to be collected by the FPA [5, 6]. For instance, inhomogeneous pixel responsivities produce a different photon-electron conversions per pixel [7] and photo-detector's dark current introduces an offset noise per pixel. Finally, at the readout electronics, typical readout architectures, such as passive-pixel sensor (PPS) or active-pixel sensor (APS), introduce both temporal and spatially patterned noises [8, 9].

The noise observed in the images rendered by PBHCs can be simply categorized, based on the noise randomness, into spatially unstructured and spatially structured noise. The spatially unstructured noise appears as a "random" noise superimposed over every monochromatic hyperspectral image, that is, no recognizable pattern is observed on top of the hyperspectral images. Examples of spatially unstructured noise are the shot noise, the dark-current noise, the electronic noise, as well as the speckle noise [4]. Conversely, the spatially structured noise is a type of noise exhibiting a well-defined spatial pattern laid over the hyperspectral images. Examples of spatially structured noise are the NU noise [10] and the striping noise (SN) [5, 6].

The SN is defined as either a periodic or an aperiodic yet partially deterministic line pattern appearing along the direction of scanning in hyperspectral images ren-

dered by PBHCs [6]. The SN, also termed as the vertical SN [5, 10], is an artifact common to push-broom scanners that severely affects the quality of the images in the hypercube. The SN is generated by one or several NUs affecting the spectrograph, the sensor, and the readout electronics sub-systems. The SN in PBHCs is mathematically represented by a set of parameters that are included in an image degradation model. A striping noise compensation (SNC) algorithm is the mathematical procedure employed to estimate the noise parameters and compensate the raw images in the hypercube.

SNC of multispectral and hyperspectral images has been conducted by means of tailored image processing algorithms. For instance, Gadallah and Csillag, [11], as well as Rakwatin *et al.*, [12], proposed SNC algorithms for multispectral push-broom cameras using statistical estimation theory. Chang *et al.* proposed a moment matching (MM) technique in conjunction with wavelet-based multiresolution analysis to compensate for the SN [13]. In addition, standard low-pass and Wavelet-transform–based filters were used to compensate for the spatial frequency components of the SN at each spectral band [14, 15]. Chen *et al.* implemented a method, based on the discrete Wavelet transform, for removing oblique SN in multispectral images. The method maps every multispectral image onto the spatial frequency domain where the noise is filtered out [16]. Following the same ideas, Münch *et al.* developed a Wavelet-Fourier spatial filter that considers a reduced number of Wavelet decomposition steps and is robust to changes in the noise pattern [17]. Remarkably, Leathers *et al.* observed that the NU noise in broadband infrared cameras is akin to the SN, and applied scene-based non-uniformity correction (NUC) algorithms to compensate for the SN in PBHCs [10]. More recently, variational methods have been considered as a viable solution for SNC under the assumption that the noise is unidirectional. Shen *et al.* proposed a maximum-a-posteriori SNC algorithm based on a Huber-Markov regularization model [18]. Also, Bouali and Ladjal proposed a SNC method that minimized the signal estimation error subject to a total-variation regularizing constraint.

It is worth noting that the aforementioned algorithms compensate for the SN using the information contained at a single spectral band; consequently, they disregard the large amount of the spectral information contained in the hypercubes. To the best of our knowledge, only in [6], [19], and [20] the SN was compensated exploiting the high

degree of correlation exhibited by neighboring bands in hyperspectral imagery. Acito *et al.* proposed in [6] a subspace-based SNC algorithm that imposed no constraints on the spatial statistical distribution of the scenes. They also assumed that the SN was not the dominant noise term. The algorithm used both the spatial and the spectral information in the hypercube to compute projection matrices. These matrices and the raw data were used to estimate the true scene and the SN components. With these estimates at hand, a polynomial-based estimator was used to determine the SN and then to compensate the spectral raw images. Sun *et al.* proposed an automatic SNC method based on spectral-domain MM estimators [19]. The method was used to compensate for the striping artifacts in the Earth-Observing-1 Hyperion imaging spectrometer. Meza *et al.* relied on the strong signal correlation at adjacent bands of PBHCs to propose a method for calculating a multidimensional (spatial and spectral) target image. This target image was, in turn, used to estimate in a recursive manner the noise parameters and ultimately to compensate for the SN [20].

Despite the fact that the use of additional spectral information is helpful during the SNC process, it carries a disadvantage in terms of how the spectral resolution is affected. In this regard, Chen *et al.* introduced a spatial-spectral domain mixing prior in a maximum a posteriori framework to compensate for Gaussian noise in hyperspectral imaging [21], minimizing the modifications in the spectral signature. However, the proposed prior is defined in terms of the first-order derivatives, limiting the spectral information only to adjacent bands. Tomasi and Manduchi in [22] propose a spatial edge-preserving bilateral filter, stating that for a pixel to influence another pixel, it should not only occupy a nearby spatial location but also have a similar intensity value. Peng *et al.* extended this concept into the spectral domain in [23], measuring the intensity differences in each spectral band to generate one spectral filter to be applied in each band. However, this approach is useful only when images are to be merged, like multispectral RGB images, not when the objective is to maintain the spectral resolution during a SNC process.

In this thesis, we present an observation model for PBHC in a comprehensive manner, understanding the optoelectronic nature of each parameter. The novelty of the model arises from: (i) assuming that the SN parameters are spatially uncorrelated and spectrally independent; (ii) decoupling the multiplicative SN parameter from the spectral response of the camera; and (iii) the capability of the model for abstracting

practical readout architectures such as APS and PPS, which are known to generate different noise patterns [8].

Consequently, two image-processing–based SNC algorithms have been developed so that they can effectively use the redundant information supplied by high spectral resolution PBHCs. The novel algorithms are termed as multidimensional due to they exploit, simultaneously, the spatial information contained in an image and the spectral information contained in adjacent spectral images. The algorithms extended here are the recursive least mean square (LMS), neural network (NN) approach by Meza *et al.* [20] and the classical MM algorithm by Gadallah and Csillag [11]. Further, a third multidimensional SNC algorithm based on bilateral filters is proposed to compensate for the reduction in spectral resolution caused by an overuse of the spectral data. The experimental assessment of the proposed multidimensional SNC algorithms has been conducted using real raw hyperspectral data collected by means of a visible (VIS) hyperspectral camera in the range of 400 to 1000 [nm] at a resolution of 1.04 [nm], and a near infrared (NIR) hyperspectral camera in the range of 900 to 1700 [nm] at a resolution of 3.06 [nm]. Hypercubes from the aforementioned PBHCs exhibit two different noise patterns, which are attributed to APS and PPS readout architectures. After conducting a theoretical analysis of the proposed algorithms, it was concluded that the spectral redundant information can be effectively used only when the SN parameters are spectrally uncorrelated. If this condition is not met, the spectral information does not increase the performance of the SNC algorithms.

1.2 Hypothesis

It is possible to model the sensor response of a hyperspectral system in a pixel-based manner considering the time, space, and spectral parameters.

1.3 Objectives

i To obtain a pixel-based model that represents the response of a hyperspectral system:

$$Y = f(X, \overrightarrow{\phi}, \overrightarrow{\theta}),$$

where $\overrightarrow{\phi}$ are the parameters of the model and $\overrightarrow{\theta}$ its restrictions.

ii To study the spectral information, analyzing the scene characteristics and any possible drift presented in the parameters.

iii To analyze the noise present in the camera, its structure, correlation and spectral dependence.

iv To integrate redundant spatial and spectral information to improve SNC algorithms.

v To develop a figure of merit to evaluate the performance of the hyperspectral acquisition model.

vi To define a neural model subject to temporal, spatial and spectral redundancy.

1.3.1 Extended Objectives

i To develop a destriping algorithm that benefits from all the information present in the data cube.

ii To design an experimental setup to acquire hyperspectral images.

1.4 Thesis Organization

This thesis deals with the study of the physical and the optoelectronic properties of hyperspectral imaging systems. In Chapter 2 a comprehensive model to fit the requirements in terms of the trustworthy system response and signal restoration is proposed. Chapter 3 describes the laboratory setups used to acquire hyperspectral data, and an experimental assessment of the model parameters is included. Next, in Chapters 4 and 5 two SNC algorithms that incorporate prior knowledge on the hyperspectral acquisition process are mathematically extended. We tested the algorithms with experimental data to evaluate their performance. Also, we proposed a third SNC algorithm to tackle the spectral resolution problem produced by the overuse of spectral information. Finally, Chapter 6 outlines the conclusions of this thesis and the future steps required to achieve a better performance on the proposed SNC algorithms.

Chapter 2

The Hyperspectral Acquisition Process

The main requirements in modern hyperspectral imaging applications are the reliability and accuracy of the acquired spatio-spectral information. In this regard, obtaining a high quality output depends on the calibration of several system components, such as the spectrograph and the imaging sensor array. In this chapter, we analyze the signal pathway in a hyperspectral imaging system and divide the basic structure of the hyperspectral camera into four sub-systems regarding the task performed by each one. Further, we discuss how each sub-system affects the signal during the photon-to-electron conversion, and identify the undesired noise sources. With this knowledge, we provide a comprehensive observation model that meets the requirements for developing effective noise compensation schemes.

2.1 The Signal Pathway

Before discussing the stages concerning the signal transduction process, we need to describe the required mechanism for collecting irradiance from a target scene. Such information is useful in identifying how the spatial and temporal dimensions are recorded within the acquired data, which in turn is essential for the mathematical modelling. In general, hyperspectral cameras can be classified into two types depending on how the acquisition of the scene is performed: i)whisk-broom and ii)push-broom cameras [24]. On one hand, the whisk-broom hyperspectral camera (WBHC)

carries out scanning by means of a set of mirrors, which rotate and sweep in a perpendicular direction of the camera movement (across track scanning). Nevertheless, due to the movement associated with the mirrors, the spatial distortion on the rendered image must to be corrected. Further, WBHCs has low spatial signal-to-noise ratio (SNR) due to limited integration time [25]. On the other hand, a PBHC has no moving parts, and the scanning procedure is performed in the direction of the camera movement (along track scanning) [26]. This type of camera offers higher integration time, hence, collecting more light and achieving larger SNR value than the WBHC. In Figure 2.1, both types of scanning technology are illustrated.

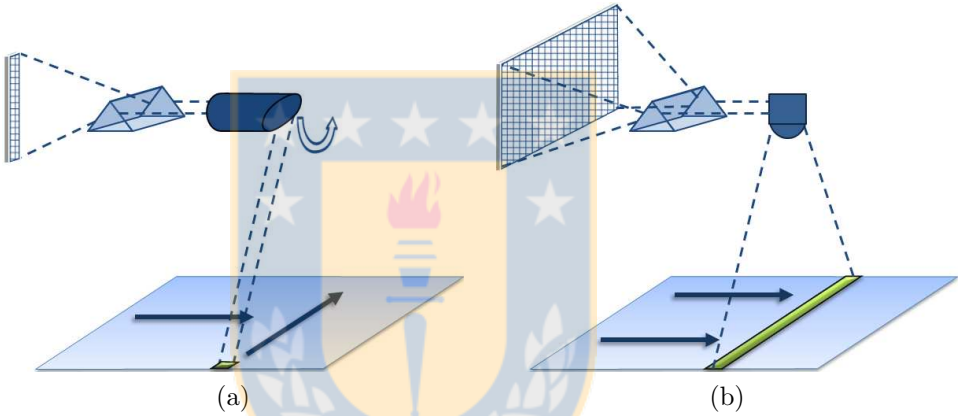

Figure 2.1: Illustration the scanning mechanism of a: a)whisk-broom hyperspectral camera and a b)push-broom hyperspectral camera works.

In this thesis we focus on PBHCs. The basic elements of PBHCs can be grouped into four sub-systems: i)the focusing optics; ii)the dispersive spectrometer; iii)the image sensor array; and iv)the readout electronics. A schematic diagram of the basic elements of a hyperspectral imager is presented in Fig. 2.2.

The front-end sub-system is the optics. Some of the problems associated with the use of a high number of lenses are reflections off lens edges, residual aberrations, including astigmatism at outer wavelengths, degraded diffracted wave-front, and a limited wavelength range that can be limited by the level of chromatic aberration correction over the operating spectral range [27]. In particular, the first set of lenses collects and focuses the incoming light onto an entrance slit that limits the area of observation to a single line, acting as a field stop view. This slit is essential to the spectrometer's performance and determines the photon flux that enters the camera.

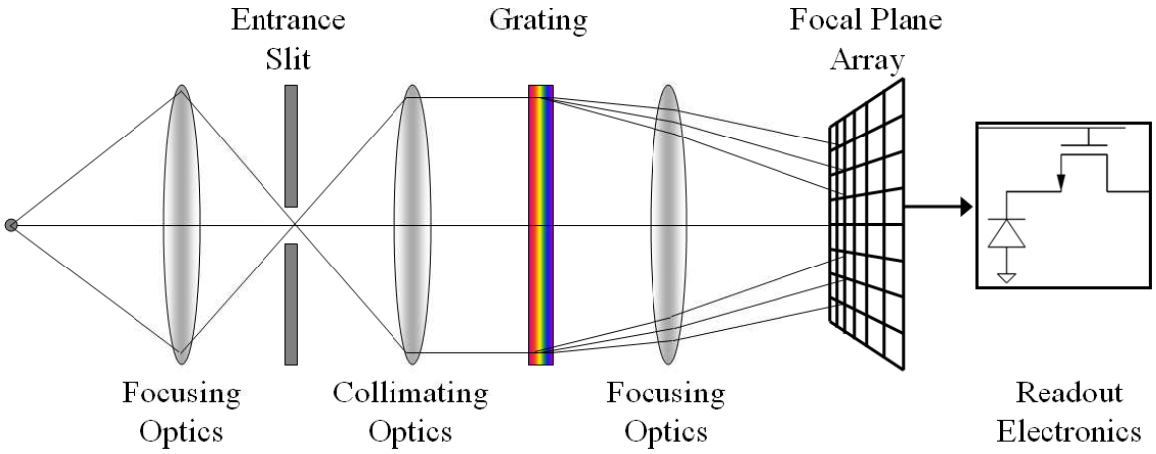

Figure 2.2: Schematic diagram of the basic elements for PBHCs.

Also, slit's purpose is to control the spectral resolution of the PBHC, that is its ability to separate close wavelengths [28]. This will be addressed again when we consider the relationship between the entrance slit and the exit slit located in the third sub-system.

After the entrance slit, a collimating optic is used to bring parallel rays to the next sub-system: the dispersive spectrometer. The dispersive element is typically a diffraction grating (although prisms may also be used) dispersing the light into its color spectrum. Both the grating and the prism induce a wavelength-dependent shift in the position of the image. In simple words, the output spectrum leaves the grating at slightly different angles, with the angles dependent upon the wavelength [29]. The further away from the grating, the distance between wavelengths increases in the dispersed radiation. At this stage, the alignment is essential since any miss calibration can produce a mixed reading between the spatial and spectral data. Then, the dispersed radiation is focused (by a second-stage of focusing optic) on the third sub-system: the sensor. This sub-system is typically a two-dimensional FPA composed of $P \times Q$ detectors that collect the spatio-spectral information of the line image by converting the photon energy into an electric charge [30]. Here, any manufacturing imperfection on the pixel active area may introduce variations in the number of photons to be collected by each detector [5,6], which becomes a significant problem when facing $P \times Q$ different responses. Also, inhomogeneous pixel responsivities produce different photon-electron conversions per pixel and photo-detector's dark current introduces an offset noise per pixel [7]. Furthermore, unlike broadband imagers, in a PBHC the spatial information is mapped onto one dimension of the FPA while

the spectral information is mapped onto the second dimension. The dispersed light spectrum impinging the FPA is mapped in Q' spectral bands, where each band is centered at the wavelength λ_j with $j = 1, \ldots, Q' \leq Q$. Similar to the concept of a monochromator, each detector row is considered as an exit slit, and their width is equal to the pixel size [31]. Hence, the instrument spectral bandpass is defined either by the entrance slit width or the pixel size in the FPA (whichever is larger) and not by the number of rows along the spectral axis of the FPA. In other words, the bandpass is set by the user, and the spectral resolution is restricted by the functional limits of the instrument. Further, the bandpass is determined when the full width at half maximum (FWHM) of a monochromatic emission line is not reduced, even when the slit width continues to be narrowed (see Fig. 2.3). If the spectral bandpass is greater than the instrument resolution, the interference between neighbouring bands increases, a phenomenon better known as spectral crosstalk.

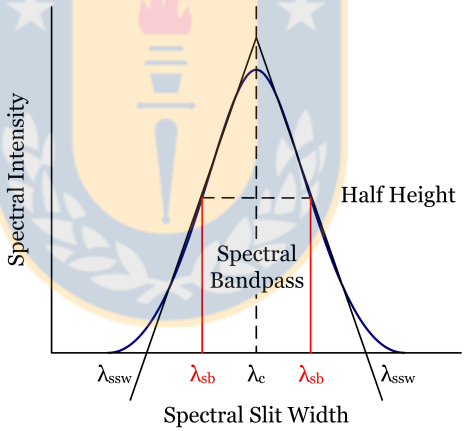

Figure 2.3: Gaussian spectral intensity distribution of wavelengths arriving to the pixel. The spectral bandpass is defined by the red boundaries and the image slit width by the black boundaries.

Ideally, the slit width should be matched to the pixel size of the FPA for optimal spectral performance. If the slit width is too narrow, then the light intensity received by the detector will be too small, and the SNR will decay [32]. Conversely, if the slit width is too large, two problems emerge: i)the spectral discrimination between spectral lines is reduced, increasing the possibility of spectral crosstalk; and ii)the SNR will be good to a point where it decreases due to the increment in continuum background emission [29]. In practical terms, an unofficial design rule recommends

matching the slit width with three pixels to avoid reducing the photon flux. It is worth mentioning that any uncontrolled variation in the slit's width introduces NU in the number of photons collected at any spectral band [5].

Finally, the readout electronics is the sub-system retrieving sensor's electric charge, converting it into a voltage signal. The signal is amplified, and ultimately, converted to digital counts at each pixel [33]. Furthermore, the amplification scheme applied on each pixel is selected depending on the application, the characteristics of the target scene and the costs involved in its construction. Kodak *et al.* presented in [34] the most popular designs in analog-digital conversion architectures, the PPS and the APS readout schemes.

i PPS sensors:

The PPS readout architecture is analogous to a simple switch in the pixel to readout the photo-diode integrated charge. In a two-dimensional structure, after addressing the pixel by opening the row-select transistor, the pixel is reset along the column bus and through the row-select transistor. Further, the amplification stage is performed at the end of each column. The schematic of the PPS scheme is shown in Fig. 2.4 where it can be noted that PPS contains a photo-diode and a transistor, known as thin film transistor (TFT). The TFT does the reset and row selection of the pixel information.

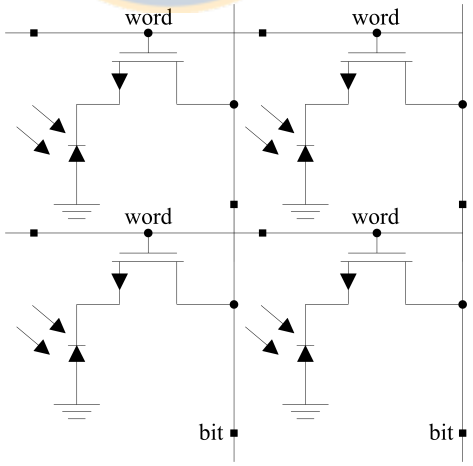

Figure 2.4: PPS structure

Since within each pixel, there is no other purpose than photon collection and conversion, the active area for photon collection is almost the entire pixel area.

Hence, this architecture achieves a high fill factor value (near 100%), which leads to a high quantum efficiency. However, the PPS scheme suffers from slow readout speed and small SNR.

ii APS sensors:

In the APS readout architecture, part of the readout electronics is designed next to the photo-detector junction within the pixel itself; hence, every pixel gets its own amplifier. This provides a preamplification of the signal and low output impedance with advantages such as i)problems of charging large parasitic capacitance of row and column buses are limited (noise reduction); ii)the time required for the readout of each pixel is shorter; iii)pixels or clusters of pixels can be separately addressed (windowing); iv)power optimization. The basic APS architecture is shown in Fig. 2.5.

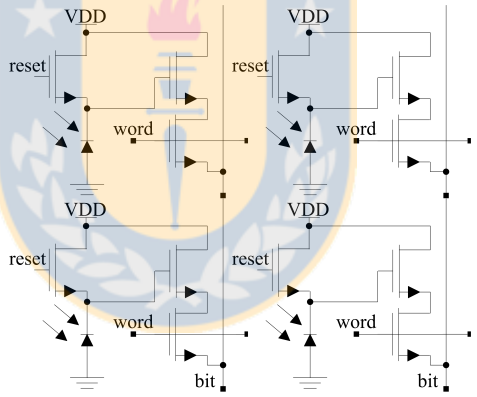

Figure 2.5: APS structure

Among the drawbacks of the APS architecture are: i)the active area for photons collection is only a fraction of the overall pixel area when compared with the PPS architecture; ii)the gain can be slightly different among different pixels due to the preamplification stage, which determines a non-uniform response between detectors at the FPA output.

Regardless of the readout scheme, the signal preamplification (be it inside or outside the single pixel) is almost always a conversion from charge to voltage. The adjustment of the signal to a digital level requires several active and passive electronic components per pixel. Ideally, these components must have the same value per pixel,

but in reality there are always slight variations. These variations introduce spatially structured noise into the signal where the pattern depends on the readout scheme [35]. Due to the column-by-column amplification used in the PPS architecture, a stripe-like pattern affect the FPA when the signal is readout. On the other hand, the pixel-by-pixel preamplification carried out in the APS architecture produce a grid-like pattern. Figure 2.6 illustrates the noise pattern observed in a two-dimensional array as a function of the analog-digital conversion scheme implemented.

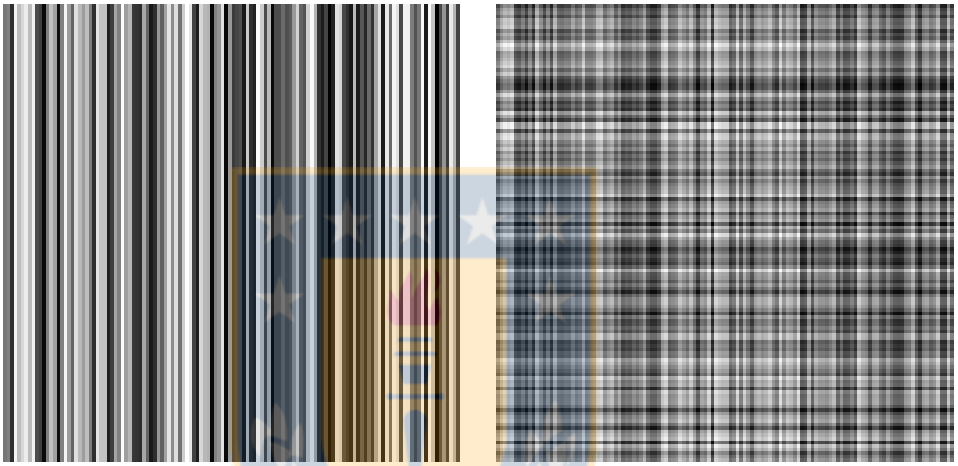

(a) (b)

Figure 2.6: Structured noise pattern presented in an FPA using a)PPS and b)APS readout architecture.

After this stage, each recorded frame is stored in a hyperspectral data cube, better known as a hypercube. In Fig. 2.7, the three dimensions recorded in the hypercube are displayed.

If the hypercube is affected by noise, each spectral image will display a striping pattern, independent of the noise pattern observed in the FPA. This is due to the assembly process of the spectral image, which requires fixing a spectral band and then appending each recorded line. Since measurements of the spectral band are performed by the same row of the FPA, the noise pattern affecting the spectral band is reflected in the final spectral image. This is explained from a mathematical point of view in the next section, where we present a model for a PBHC.

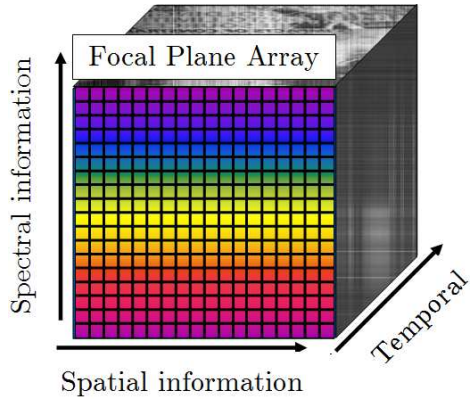

Figure 2.7: Basic hypercube structure.

2.2 Observation Model for a Push-broom Hyperspectral Camera

Based on the characteristics of a PBHC exposed in the previous section, let us consider a PBHC equipped with a FPA composed of $P \times Q$ photo-detectors. Suppose that, at a given sample time, only one spatial line from a given target scene is mapped by the camera onto a P-dimensional vector. Suppose also that, for each element in such vector, the spectrograph generates a Q'-dimensional vector with the spectrum of each spatial sample, where $Q' \leq Q$. Furthermore, suppose that the target scene is completely imaged in the spatial domain by acquiring S lines at consecutive sample times. For the sake of notation, from now on a spatial position on the FPA shall be denoted using either ij or (i, j), and a spatial position on the target scene shall be denoted as ik.

In this thesis, the digital output of the PBHC, $Y(i, \lambda_j, k)$, which corresponds to the observed input irradiance at ikth spatial location of the target scene and at the λ_j spectral band (or wavelength), is modeled as:

$$Y(i, \lambda_j, k) = r(\lambda_j)a(i, j)X(i, \lambda_j, k) + b(i, j) + V(i, j, k), \tag{2.1}$$

where $i = 1, \ldots, P$, $j = 1, \ldots, Q$, $k = 1, \ldots, S$, $X(i, \lambda_j, k)$ is the true input irradiance at the ikth spatial location of the target scene and at the λ_j spectral band, $V(i, j, k)$ is an additive spatial white noise associated with the readout electronics of the ijth photo-detector, $r(\lambda_j)$ is the overall spectral response, and $a(i, j)$ and $b(i, j)$ are param-

eters representing the SN at the ikth pixel of the hyperspectral image sampled at λ_j wavelength. The terms $a(i,j)$ and $b(i,j)$ represent, respectively, all the multiplicative (gain) and additive (offset) noise sources corrupting the output of a PBHC.

For the proposed observation model, in Eq. (2.1), the following set of assumptions has been made. First, the input irradiance of the target scenes is assumed to be a continuous, fairly smooth function of the wavelength. Second, the overall spectral response of the camera is assumed to be a known-parameter, which is either supplied by the camera manufacturer or can be experimentally characterized. Third, we impose the practical assumption that the white noise $V(i,j,k)$ is negligible compared to the offset $b(i,j)$. Fourth, the SN parameters $a(i,j)$ and $b(i,j)$ are assumed to be spectrally independent yet dependent upon the spatial location of a photo-detector in the FPA. The former assumption is justified by the fact that the main SN sources are wavelength independent [36] while the latter assumption is commonly made in the literature. It must be commented that, in some PBHCs, the SN pattern appears to be inhomogeneous over the wavelengths; however, such inhomogeneity is not generated by any spectral-dependent effect but mainly by the readout electronics as, for instance, in the case of APS architectures [8].

The observation model in Eq. (2.1) differs in various aspects when compared to other first-order models used in the literature: i)the first-order model traditionally used is based on a single-image processing approach where the spectral dimension is disregarded (*cf.* Eq. (1) in [37], Eq. (2) in [38], Eq.(1) in [39]); ii)other first-order models do not decouple the spectral response from the multiplicative term associated with the striping noise (*cf.* Eq. (5) in [36], Eq. (1) in [40]); iii)another class of models considers a signal-dependent and an additive striping noise parameter (*cf.* Eq. (1) in [41]); iv)yet another model incorporates additional PBHCs' sub-systems, such as the blurring effect produced by the optical sub-system (*cf.* Eq. (3) in [42]).

The novelty of the observation model can be summarized as: (i) regarding the SN parameters as spatially dependent yet spectrally independent, and (ii) including the overall spectral response of the FPA. Note that this new representation for the observation model allows us to think of $r(\lambda_j)$ as a striping-noise–free parameter that models ideally all the multiplicative effects in the spectral response, while the term $a(i,j)$ takes into account all the multiplicative SN sources. Note also that the notation emphasizes the spatial and/or spectral dependence of each term by clearly

distinguishing between a spectral band, λ_j, and its column number in the FPA, j.

It is worth mentioning that the SN can be observed in a mathematical fashion. To observe this effect, first the variable j is dropped from the analysis by fixing a spectral band. Second, a spatially and temporally flat input, i.e., $X(i,k) = x_0$ for all i and k is assumed. With this, the image assembled by the PBHC at a fixed band is the collection of pixel values $\{Y(i,k) : Y(i,k) = a(i)x_0 + b(i)\}$, which clearly represents a flat image corrupted by horizontal or vertical stripes. The orientation depends on the scanning direction.

2.3 Summary

We have detailed the signal pathway through a PBHC, describing how the signal is physically modified by each component and how it is affected by different noises sources. In this case, we can say that the most critical stages of the process are the dispersive spectrometer and the image sensor array, decomposing the input radiation and performing the photon-electron conversion, respectively. Furthermore, noises affecting signal were analysed in terms of their sources and pattern structures, which can be described as stripe-like or grid-like noise patterns. Here, we emphasize that the dominant source of structured noise is the readout electronics, where the electrical design scheme is a determinant characteristic of the pattern observed. We have derived a first order model for a PBHC where each parameter is carefully defined in terms of its properties and dependencies. In order to maintain the physical coherence of the proposed model, we separate the multiplicative parameter into two terms, abstracting all the effects that are wavelength-dependent from the effects that are positionally-dependent. Also, we define the noise parameters to model structured patterns that can affect the FPA, hence, such structures can be seen as a representation of the electronic design.

Chapter 3

Analysis of the Model Parameters

In this chapter, a detailed model parameter analysis through experimental characterization of PBHCs is performed. The conclusions obtained here validate the assumptions suggested by the observation model presented in Chapter 2. Finally, the required experimental setups are designed, based on calibration procedures using devices such as spectrally uniform lamps, diffuse reflection surfaces, etc., elements that are described in Appendix B.

3.1 Experimental Setup

In order to assess the theory expressed in Chapter 2, we analyze the PBHC spectral response, bandpass and noise parameters employing the setups illustrated in Fig. 3.1. These setups are composed of two different hyperspectral cameras. The first one operates in the NIR spectral range, between 900-1700 [nm], with a nominal spectral resolution of 3.64 [nm]. This camera is composed of a $P = 320$ and $Q' = 256$ InGaAs photo-diode array with a PPS readout architecture, which allows to obtain $Q = 236$ spectral bands. The second camera operates in the VIS spectral range, between 400-1000 [nm], with a nominal spectral resolution of 2.73 [nm]. The FPA is composed of a $P = 1024$ and $Q' = 1024$ CMOS array with an APS readout architecture, with $Q = 574$ readable spectral bands. Also, to render spectral images from the raw data, the target is mounted on a linear-stage platform to simulate the along-track scanning procedure of practical PBHCs, whose travel speed is synchronized with the camera integration time.

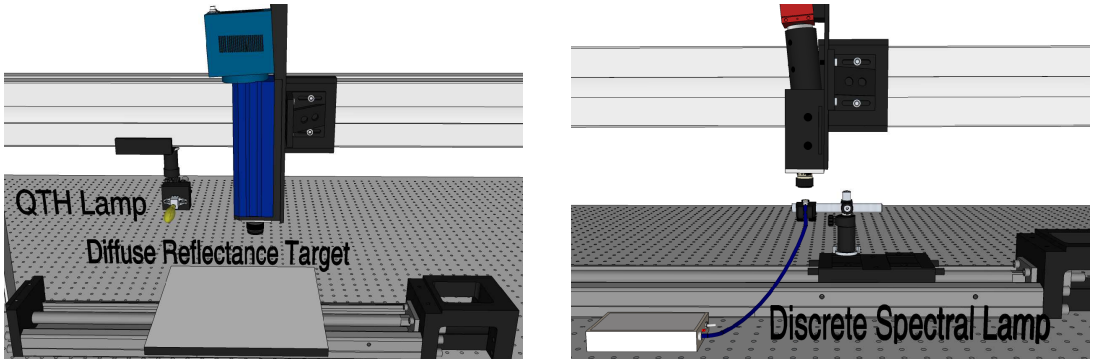

(a) (b)

Figure 3.1: a) Laboratory prototype to retrieve the system spectral response and to analyse the noise patterns. b) Laboratory prototype to study the spectral crosstalk.

The calibration device employed in our setup is a quartz tungsten halogen (QTH) lamp, which guarantees an uniform and continuous spectral illumination between 200-2500 [nm] with a programmable input power between 200-1000 [W]. Further, we use a Spectralon SRT-99-120 as a diffuse reflectance target that ensures a reflectance of 99% between 250-2000 [nm] (see Fig. 3.1.a). Finally, we use two discrete spectral emission lamps to characterize the spectral resolution of both cameras (see Fig. 3.1.b). It should be noted that most emission lines of these calibration lamps have a line width of less than 0.001 [nm], which is less than the resolution of the optical systems.

3.1.1 System Spectral Response

The response of the elements which in combination generate the system spectral response of a PBHC are: i) the optics; ii) the dispersive spectrometer; iii) the spectral responsivity of the detector material. Here, we measured the spectral response for each camera by employing the QTH lamp, which provides a spectrally uniform illumination in the operational spectral range for both cameras (using the set-up described in Fig. 3.1.a). The light impinges the SRT-99-120 surface, producing a diffuse reflection in the operating spectral range, obtaining a uniform illumination in spectrum and space. Each hypercube is 500 frames long and then averaged over time and space to compensate for random noise. Finally, we present the resulting response curve for the VIS and NIR hyperspectral cameras in Fig. 3.2. It must be remarked that, for the VIS camera, the abnormal fluctuations observed in Fig. 3.2.a are generated by

the fluctuating photonic response of the CMOS FPA detector as described in Photon Focus Inc. [43].

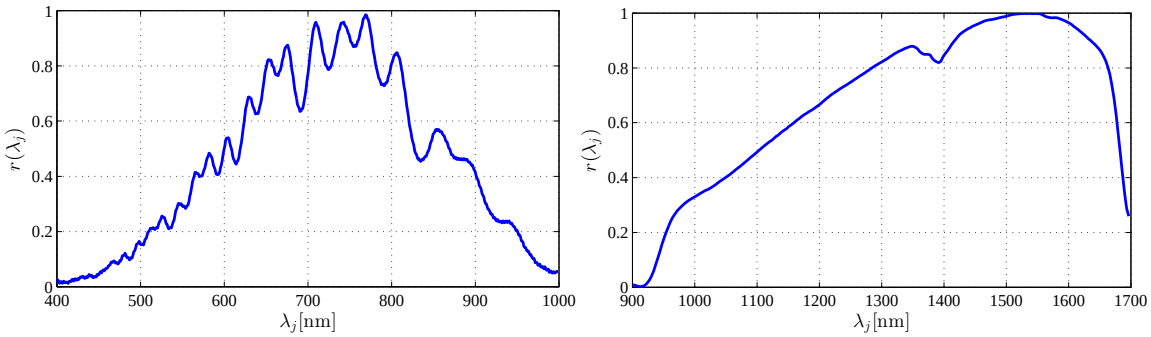

(a) (b)

Figure 3.2: System spectral response for the a) VIS and b) NIR hyperspectral cameras.

Unlike the VIS camera, the spectral response curve obtained for the NIR hyperspectral camera can be considered smoother along its spectral response, however, it is observed a more sudden decrease at lower and higher spectral bands. It must be emphasized that the number of bands is less than the amount of column detectors due to the responsivity of the semiconductor material. That is, the effective spectral range is displayed on a smaller area than the FPA; hence, the column detectors located at the edges of the FPA are disabled.

3.1.2 Nonuniformity Noise

In Section 2.2, the noise parameters are defined by the terms $a(i, j)$ (gain) and $b(i, j)$ (offset). The calibration procedure conducted here consists in generating three reference points to determine the three parameters in Eq. (2.1). The first reference point corresponds to a dark reference value for determining the offset level $b(i, j)$. This reference point can be obtained by blocking the camera input. This is further justified because the radiation emitted by the blocking object is not detectable in either VIS or NIR spectral range. Figure 3.3 shows the offset acquired for both cameras.

Both experimental offsets were calculated from a hypercube of 500 frames long, where each hypercube is averaged in time to reduce the temporal electronic noise ($V(i, j, k)$). The stripe-like noise pattern observed in Fig. 3.3.b corresponds to what

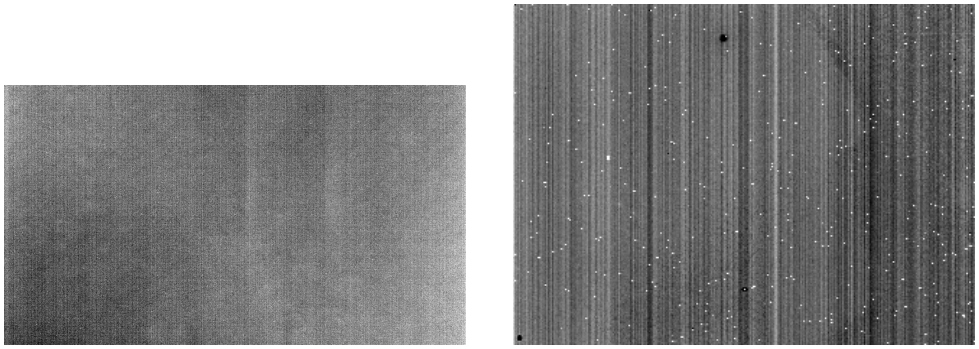

(a) (b)

Figure 3.3: Experimental offset level for the a) VIS and b) NIR hyperspectral camera.

is expected when dealing with PPS readout architecture. It should be remarked that this type of pattern exhibits a high correlation in the spectral domain. Similarly, the grid-like pattern in Fig. 3.3.a resembles the pattern observed in cameras with an APS readout architecture.

Furthermore, the other two reference points correspond to two different light intensities, which are reflected by the Spectralon target to obtain the gain $a(i, j)$ and the overall spectral response $r(\lambda_j)$. Several works have stated that, in many operational conditions, the offset level overshadow the gain level [44–46]. In this regard, by comparing the experimental values obtained for both parameters, we observe that the variation for the offset are greater than the variation of the gain parameter. In Fig. 3.4 the gain level acquired for both cameras is presented.

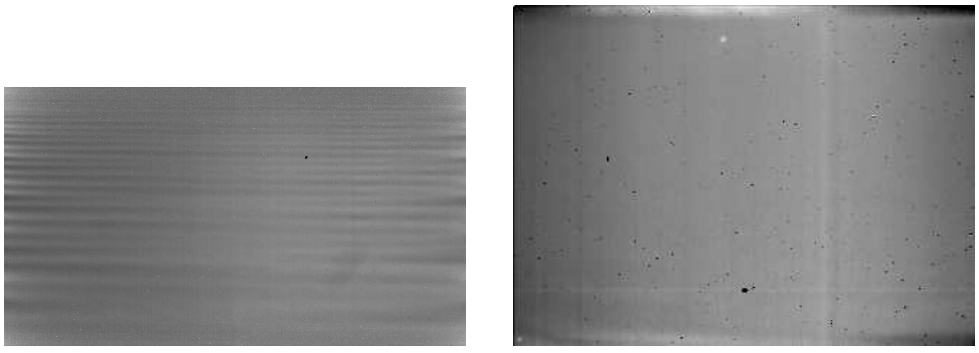

(a) (b)

Figure 3.4: Experimental gain level for the a) VIS and b) NIR hyperspectral camera.

It should be noted that the fluctuations observed at the edges of Fig. 3.4.a are attributed to minor estimation errors in the spectral response.

Moreover, in this thesis we have stated that the noise parameters do not change over a period of time (drift). To support this assumption, a study is performed on the noise parameters in terms of its temporal variation. Since the offset variation are greater than the gain variation, we will analysis only the temporal characteristics for the offset value, and we will determine if there is any significant variation over time that may affect the noise compensation process. In Fig. 3.5, the response of 9 neighbouring pixels randomly selected is shown, where each point of the curve is the temporal average of the selected pixels. Further, noise measurements were conducted using both cameras, with a time frame between measurements of 1 hour. The experimental conditions for each measurement were the same: i) room temperature of 21^o C; ii) the integration time for VIS and NIR cameras was fixed at 178 ms and 20.3 ms, respectively; and iii) each hypercube was 300 frames long. It is worth mentioning that, unlike the VIS camera, the NIR camera has an integrated cooling system that was set to 10 ^{o}C.

From Fig. 3.5, we note that detectors's response for each camera follows a similar trend in time. This trend can be attributed to internal thermal variations of each camera, which emphasizes the harmful effect that uncontrolled variations in ambient temperature could have on the detectors response. Regardless of this effect, it can be seen (in both figures) that the response of each detector varies over time with a temporal deviation of less than 1% of the dynamic range, for each camera. Hence, the assumption that the parameters defining the noise are time-invariant, during the a window of time, remains valid.

3.1.3 Spectral Dependence

The results obtained in Sections 3.1.1 and 3.1.2 allow us to conduct an analysis on the spectral dependence for the SN parameters. From Section 2.2, noise sources modeled by the gain $a(i,j)$ and offset $b(i,j)$ are not spectrally dependent; hence, it is expected that these results will support our research.

Figure 3.6 presents both parameters, the estimated gain and offset SN parameters averaged over the spatial dimension for each camera, i.e. $\bar{a}(j) = P^{-1}\sum_{i=1}^{P} a(i,j)$ and $\bar{b}(j) = P^{-1}\sum_{i=1}^{P} b(i,j)$. Roughly speaking, Fig. 3.6.a shows that both parameters have, on average, no spectral dependence for the VIS camera. These

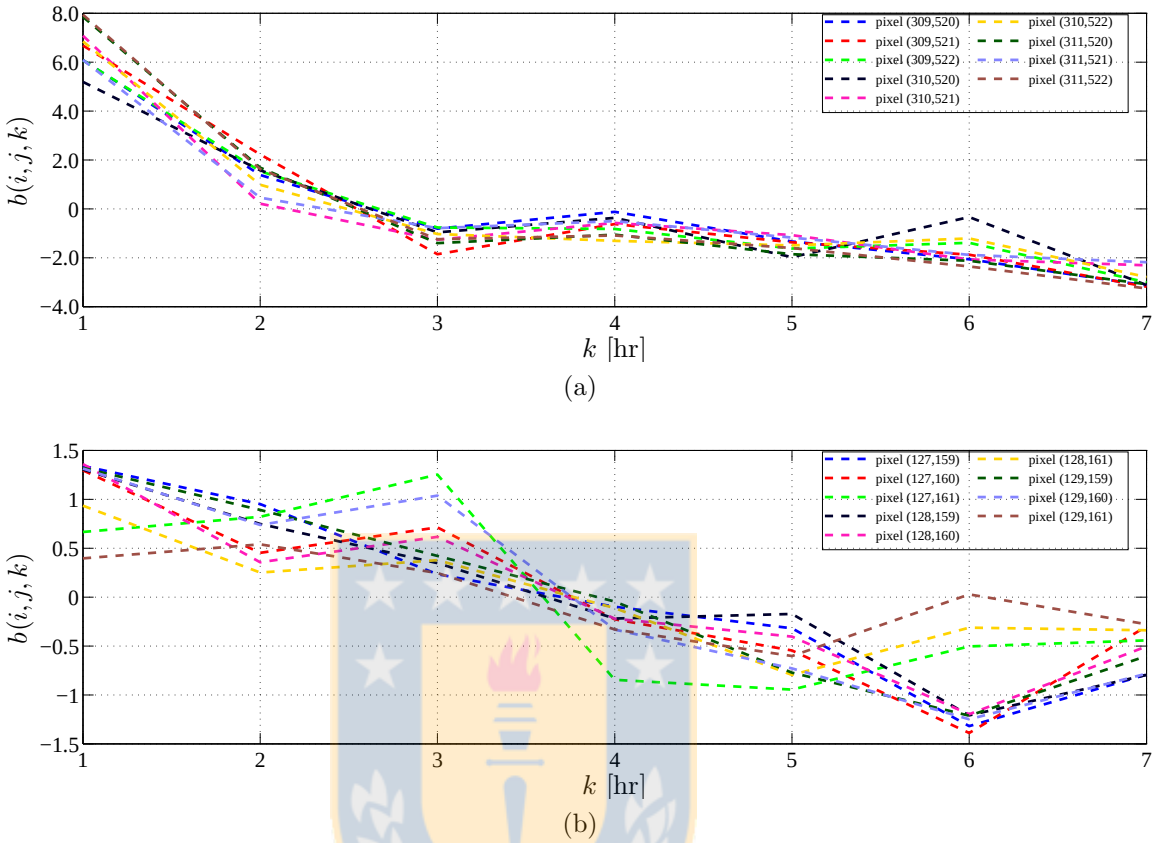

Figure 3.5: Temporal drift response of 9 neighbouring pixels for the a) VIS and b) NIR hyperspectral cameras.

results support also that SN parameters are spatially dependent to the detector position. The average gain parameter is $m_a = \sum_{j=1}^{Q} \bar{a}(j)/Q = 1.0$ with a standard deviation of $\sigma_a = \sqrt{\sum_{j=1}^{Q}(\bar{a}(j) - m_a)^2/(Q-1)} = 0.09$, and the average offset parameter is $m_b = \sum_{j=1}^{Q} \bar{b}(j)/Q = 411.8$ with a standard deviation of $\sigma_b = \sqrt{\sum_{j=1}^{Q}(\bar{b}(j) - m_b)^2/(Q-1)} = 71.65$.

A deeper statistical analysis of the data shows also that the variance of the offset parameter is fairly homoscedastic along the band number, while the variance of the gain parameter shows heteroscedasticity at the lowest and the highest band numbers. This behavior is attributed to the fact that, at the lowest and highest spectral bands, the overall spectral response of the system is close to zero and the spatial variations in the gain increase due to the lowest signal-to-noise ratio.

In Fig. 3.6.b, the NIR camera exhibits SN parameters with a marked spectral

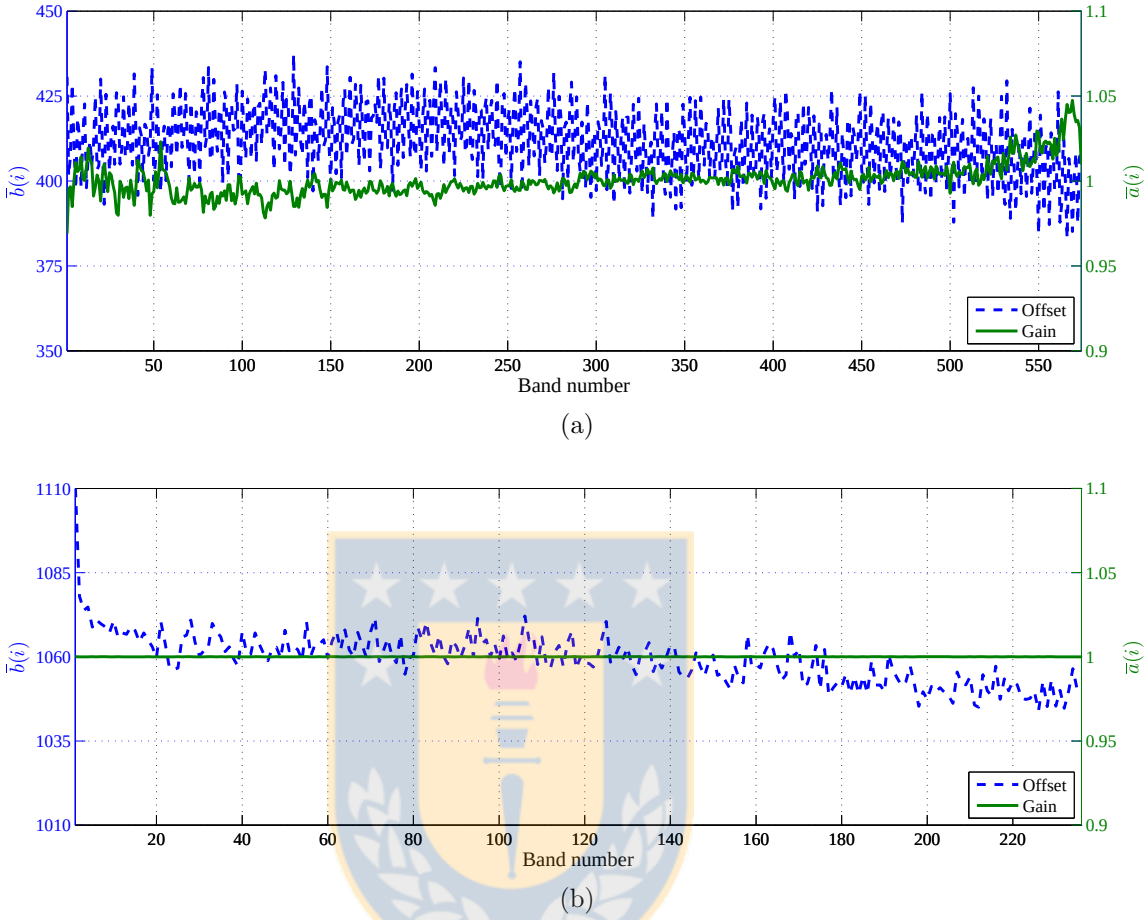

Figure 3.6: Spectral analysis of the gain and offset parameters for the a) VIS and NIR hyperspectral cameras.

dependence. These results are in agreement with the design of a PPS readout architecture. The average gain parameter is $m_a = 1.0$ with a standard deviation of approximately $\sigma_a = 0$. The low value of the gain standard deviation corroborates that the gain parameter remains practically constant at the different spectral bands. Similarly, the average offset parameter is $m_b = 1059.4$ with a standard deviation of $\sigma_b = 7.66$. It should be noted that the outliers observed in the offset are due to saturated and dead pixels. Although the offset curve was obtained through a spatial average, these values differ considerably from the rest, shifting the average value.

3.1.4 Spectral Bandpass

The spectral bandpass and resolution indicate the limits of instrument's ability to separate adjacent spectral information, where the smallest possible bandpass is the spectral resolution. Further, the spectral bandpass is directly related with the contamination between neighboring bands (spectral crosstalk). That is, the spectral bandpass represents the system response when excited by a monochromatic light source, hence, hyperspectral systems with a large spectral bandpass are affected by spectral crosstalk when acquiring radiance [47, 48]. However, this problem can be avoided by combining the spectral data from a group of pixels into a single pixel (pixel binning), limiting the spectral resolution but increasing the SNR.

The two hyperspectral cameras at our disposal are described by the manufacturer with a low spectral bandpass and the crosstalk can be neglected. To corroborate this, we intend to determine the spectral bandpass FWHM of both cameras by using the following expression:

$$FWHM = AWD \cdot W_{exap}, \tag{3.1}$$

where AWD is the average linear wavelength dispersion (in [nm/mm]) at a specific wavelength and it is calculated as the ratio between the spectral range of the camera versus the length of the pixels column; W_{exap} is the pixel size or the image width of the entrance aperture (slit image), whichever is greater. According to the collected information from the manufacturer company (see Appendix B), the width of the image for the entrance aperture covers approximately three and one pixel for the VIS and NIR camera, respectively. Such low values indicate that the spectral crosstalk is not an issue in both cameras. To experimentally verify this statement, we used two discrete spectral lamps connected to an optical fiber, Hg-1 (UV-VIS) and Ar-1 (NIR). These types of lamps provide discrete illumination in a small area to theoretically illuminate one spectral band on the FPA. Therefore, the acquired hypercube contains details on how the incident radiation has spilled out in neighbouring bands on the FPA. The results obtained using this type of lighting are presented in Fig. 3.7.

For each measurement, we selected the lines closest to the center wavelength of a particular band. Also, we compensated both spectral lines in terms of their respective offset levels and spectral gain. For the VIS camera, the spectral line in band 147 (546 [nm] line) is selected, which produces a spectral crosstalk equal to [0.30 0.41 0.29]

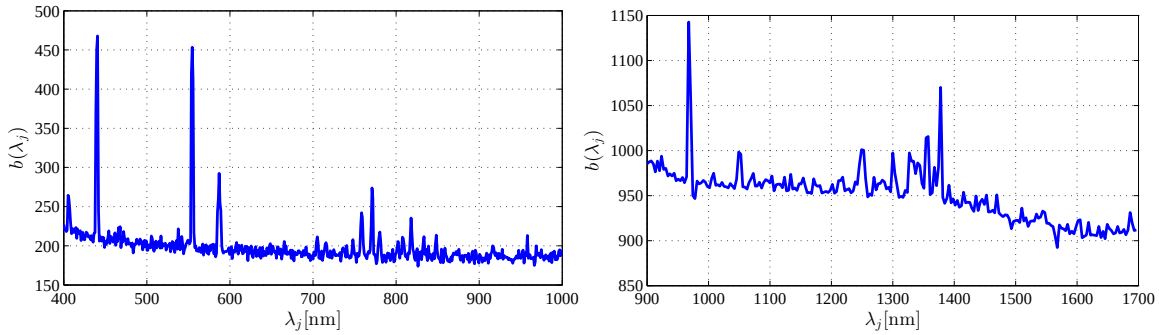

Figure 3.7: Spectral response for the a)VIS and the b)NIR hyperspectral cameras when using discrete illumination.

(normalize response for the bands 146 to 148). The rest of the neighbouring bands has intensity values similar to the noise level.

For the NIR camera, we selected the spectral line in band 21 (965 [nm] line), producing a spectral crosstalk equal to [0.20 0.54 0.26] (normalize response for the bands 20 to 22). In this case, we can appreciate a center intensity value higher than in neighbouring bands, which indicates a higher concentration of spectral information in a single pixel (band).

Finally, we have that the theoretical FWHM is approximately equal to 3.1 [nm] and 3.4 [nm] for the VIS and NIR camera, respectively. Both values are similar to those presented in the datasheet of the cameras but, it must be stressed that the spectral bandpass was calculated from average values.

3.2 Summary

The results obtained support the assumptions made in Chapter 2 related to the proposed observation model. Specifically, the idea of decoupling the multiplicative effect, generated by the conjunction of all the optoelectronic components, into spectral and noise parameters. Further, the heterogeneous behaviour of the noise parameters observed in Fig. 3.6 confirms that the intensity value read by a detector depends only on their spatial location in the FPA.

Moreover, the assumption that the SN parameters are deterministic and remain constant during a time window remains valid. Namely, Fig. 3.5 shows that the

variations in the intensity value from 9 individual pixels, during a time frame of 7 hours, are less than 1%. Nevertheless, this value may increase if cameras are under uncontrolled environmental conditions.

It is worth mentioning that the spectral crosstalk can be overlooked due to the low value observed in both PBHC. Such problems are usually compensated through hardware modifications as pixel binning or subsampling. Hence, we disregard this effect due to the low influence in the spectral response of the cameras at our disposal.

Chapter 4

Multidimensional Striping Noise Compensation

In this chapter, an extension over the spectral domain of two SNC algorithms is presented. The objective is to take advantage of the high spectral resolution provided by the hyperspectral imaging system, which entails a high spectral redundancy in the acquired hypercube. Thus, the massive spectral information available is included on the extended SNC process, increasing its effectiveness. Also, the dependency between the spectral redundancy and the structure of noise patterns during the SNC process is studied. Furthermore, we discuss the diminishing effects on the spectral resolution when the proposed compensation schemes are applied and an alternative algorithm to compensate for this problem is also proposed.

4.1 Spectral Redundancy and Multidimensional Striping Noise Compensation Algorithms

It is well-known that hyperspectral data cubes generated by high resolution PBHCs contain highly redundant spatial and spectral data [49, 50]. The spatial and spectral redundancy are manifested in the large amount of spatial and spectral correlation exhibited at adjacent spatial pixels and spectral bands. Most of the SNC algorithms rely solely on the redundant spatial information contained in the hyperspectral images and, consequently, process each hyperspectral images independently. Here, the spec-

tral redundancy has also been exploited to develop two SNC algorithms that already take advantage of the spatial redundancy; the modified algorithms take advantage of both the spatial and spectral redundant information available in the hypercubes.

The first SNC algorithm modified in this thesis is the NN-based approach in [20], which was inspired by the work of Scribner *et al.* [51]. The NN-based algorithm uses a retina-like processing technique to exploit the spatial redundancy exhibited by neighboring pixels in an image. More precisely, the retina-like technique considered the pixel wise computation of a target value at the λ_j spectral band, $\overline{X}(i,\lambda_j,k)$, as the spatial average $\overline{X}(i,\lambda_j,k) = 1/(2\Delta I+1)\sum_{u=i-\Delta I}^{i+\Delta I}\hat{X}(u,\lambda_j,k)$, where $2\Delta I+1$ is the size of the spatial neighborhood.

The spectral redundancy concept can be used to extend the definition of such target values to the following multidimensional definition:

$$\overline{X}(i,\lambda_j,k) \triangleq \frac{1}{(2\Delta I+1)(2\Delta J+1)}\sum_{u=i-\Delta I}^{i+\Delta I}\sum_{v=j-\Delta J}^{j+\Delta J}\hat{X}(u,\lambda_v,k), \tag{4.1}$$

where $2\Delta J+1$ is the number of adjacent spectral bands satisfying the spectral redundancy.

The SN parameters can be recursively estimated solving for $X(i,\lambda_j,k)$ in Eq. (2.1) and considering the multidimensional target value calculation in Eq. (4.1). Thus, the following expressions are obtained:

$$\hat{X}(i,\lambda_j,k+1) = \frac{\hat{g}(i,j,k)}{r(\lambda_j)}Y(i,\lambda_j,k) + \frac{\hat{o}(i,j,k)}{r(\lambda_j)}, \tag{4.2}$$

$$\hat{g}(i,j,k+1) = \hat{g}(i,j,k) - \eta_g(\lambda_j)\left[\frac{\left(\overline{X}(i,\lambda_j,k) - \hat{X}(i,\lambda_j,k)\right)Y(i,\lambda_j,k)}{r(\lambda_j)}\right], \tag{4.3}$$

$$\hat{o}(i,j,k+1) = \hat{o}(i,j,k) - \eta_o(\lambda_j)\left[\frac{\overline{X}(i,\lambda_j,k) - \hat{X}(i,\lambda_j,k)}{r(\lambda_j)}\right], \tag{4.4}$$

where $a(i,j) = 1/g(i,j)$, $b(i,j) = -a(i,j)/o(i,j)$, $\hat{g}(i,j,k)$ and $\hat{o}(i,j,k)$ are, respectively, estimates of $g(i,j)$ and $o(i,j)$ after k iterations, and $\eta_g(\lambda_j)$ and $\eta_o(\lambda_j)$ are spectrally-dependent learning rates defined to speed up the convergence time of the recursive estimation algorithm. These spectrally-dependent learning rates must be adjusted according to the spectral information contained in the target scene.

It should be noted that the extension in the spectral domain carries out two major modifications on the Scribner algorithm: (i) Equation (4.1) corresponds to a generalization of the unidimensional target computation presented in [51]; and (ii) the spectrally-dependent learning rates are also a generalization of the original learning rates defined for broadband imagers.

The second SNC algorithm modified in this thesis is the classical MM approach proposed by Gadallah and Csillag in [11]. They claim that, if sensors differ only in the gain and offset, these values can be estimated using the MM assumption: The mean and standard deviation of sub-scenes are similar between each other. Further, due to the lack of statistical information of the input irradiance, Gadallah and Csillag use a random sensor as statistical reference. Following the rationale of the MM assumption, it is claimed here that, along the scanning direction, the temporal first and second order statistics of the irradiance of a spectral image, $m_X(i,\lambda_j)$ and $\sigma_X(i,\lambda_j)$, remain constant and can be estimated using the spectrally redundant information contained at neighboring spectral bands. Further, it is supposed also that proper estimators for such statistics are the sample mean and the sample standard deviation taken over a subset of $2\triangle J+1$ bands centered at λ_j. More precisely:

$$m_X(i,\lambda_j) \sim \overline{m}_Y(i,\lambda_j) = \frac{1}{2\triangle J+1}\sum_{v=j-\triangle J}^{j+\triangle J} m_Y(i,\lambda_v), \tag{4.5}$$

$$\sigma_X(i,\lambda_j) \sim \overline{\sigma}_Y(i,\lambda_j) = \frac{1}{2\triangle J+1}\sum_{v=j-\triangle J}^{j+\triangle J} \sigma_Y(i,\lambda_v), \tag{4.6}$$

where $m_Y(i,\lambda_j)$ [correspondingly, $\sigma_Y(i,\lambda_j)$] is the temporal mean (correspondingly, the temporal standard deviation) of the digital output and $\triangle J > 0$.

After some algebraic manipulation of Eq. (2.1), the following noise parameter estimates can be derived:

$$\hat{a}(i,j) = \frac{\sigma_Y(i,\lambda_j)}{r(\lambda_j)\overline{\sigma}_Y(i,\lambda_j)}, \tag{4.7}$$

$$\hat{b}(i,j) = m_Y(i,\lambda_j) - r(\lambda_j)\hat{a}(i,j)\overline{m}_Y(i,\lambda_j). \tag{4.8}$$

Next, by plugging Eqs. (4.7) and (4.8) in Eq. (2.1) and solving for $X(i,\lambda_j,k)$,

the following estimator can be obtained:

$$\hat{X}(i,\lambda_j,k) = \frac{\sigma_Y(i,\lambda_j)}{\overline{\sigma}_Y(i,\lambda_j)}\big(Y(i,\lambda_j,k) - m_Y(i,\lambda_j)\big) + \overline{m}_Y(i,\lambda_j). \tag{4.9}$$

Observing the ratio of similarity between the variances leads to the conclusion that the lack of variability in the spectral domain diminishes the SNC effect of the multidimensional algorithm because solely the temporal and spectral averages are considered in the compensation.

4.2 Correlation in the Noise Parameters and its Effect on the Spectral Redundancy

Traditional SNC algorithms use a single spectral image and rely on the spatial variability provided by the scene being imaged. Any effective multidimensional SNC algorithm using the raw spatial and spectral data to filter out the SN must rely also on the variability contained in the raw spectral data. Note that when the model (2.1) is constrained by the spectral redundancy assumption, the spectral variability in the raw data must be provided by the noise parameters. In other words, in a subset of spectral bands fulfilling the spectral redundancy assumption, the spectral irradiance can be considered approximately the same. Therefore, variability in the raw spectral data can only be achieved when the SN parameters in Eq. (2.1) are uncorrelated.

The SN parameters in PBHCs can be regarded as uncorrelated when the readout electronics is implemented using an APS architecture [8]. This claim is supported by the fact that, for such architectures, every photodetector in the FPA has its own signal amplifier. It is worth mentioning here that the noise parameters of PBHCs employing PPS readout architectures can be regarded as correlated, because their photodetectors share electronic signal amplifiers. Thus, the previous claims and their effects on the proposed algorithms are formally supported. To this end, both, the spectral redundancy assumption and the lack of correlation in the SN parameters have been modeled, and their impact on the multidimensional SNC algorithms presented in Section 4.1 is analyzed.

First, let us consider the NN-based SNC algorithm and note that the spectral

redundancy assumption states that $X(i,\lambda_j,k) \approx X(i,\lambda_v,k)$ for $j-\triangle J \leq v \leq j+\triangle J$. By plugging Eq. (2.1) and (4.1) in (4.2) and after some algebraic manipulation, the following expression can be obtained:

$$\overline{X}(i,\lambda_j,k) = \frac{1}{(2\triangle I+1)} \sum_{u=i-\triangle I}^{i+\triangle I} \left[X(u,\lambda_j,k-1) \sum_{v=j-\triangle J}^{j+\triangle J} \frac{\widehat{g}(u,v,k-1)a(u,v)}{(2\triangle J+1)} + \sum_{v=j-\triangle J}^{j+\triangle J} \frac{\widehat{g}(u,v,k-1)b(u,v)}{r(\lambda_v)(2\triangle J+1)} + \sum_{v=j-\triangle J}^{j+\triangle J} \frac{\widehat{o}(u,v,k-1)}{r(\lambda_v)(2\triangle J+1)} \right]. \tag{4.10}$$

Equation (4.10) shows the spectral averaging effect that the multidimensional SNC algorithm performs over the estimates $\widehat{g}(i,j,k)$ and $\widehat{o}(i,j,k)$, which ultimately mitigates the impact of the SN on the compensated images. As a special case, let us consider a situation where the noise parameters are highly correlated in a subset of spectral bands. This situation is modeled setting $a(u,v) = a(u)$ and $b(u,v) = b(u)$, and consequently, $\widehat{g}(u,v,k-1) = \widehat{g}(u,k-1)$, $\widehat{o}(u,v,k-1) = \widehat{o}(u,k-1)$. Therefore, for this special case Eq. (4.10) simplifies to:

$$\overline{X}(i,\lambda_j,k) = \frac{1}{(2\triangle I+1)} \sum_{u=i-\triangle I}^{i+\triangle I} \left[X(u,\lambda_j,k-1)\widehat{g}(u,k-1)a(u) + \widehat{g}(u,k-1)b(u) \sum_{v=j-\triangle J}^{j+\triangle J} \frac{1}{r(\lambda_v)(2\triangle J+1)} + \widehat{o}(u,k-1) \sum_{v=j-\triangle J}^{j+\triangle J} \frac{1}{r(\lambda_v)(2\triangle J+1)} \right], \tag{4.11}$$

where one can easily observe that there is no spectral averaging over the noise parameters.

For the MM algorithm, recalling Eq. (4.5) and calculating the averaged spectral information in a subset of bands $2\triangle J+1$ centered in λ_j, the following is obtained:

$$\begin{aligned} \overline{m}_Y(i,\lambda_j) &= \frac{1}{2\triangle J+1} \sum_{v=j-\triangle J}^{j+\triangle J} m_Y(i,\lambda_v) \\ &= \frac{1}{2\triangle J+1} \sum_{v=j-\triangle J}^{j+\triangle J} r(\lambda_v)a(i,v)m_X(i,\lambda_v) + b(i,v) \end{aligned}$$

$$= \frac{1}{2\triangle J+1}\sum_{v=j-\triangle J}^{j+\triangle J} r(\lambda_v)a(i,v)m_X(i,\lambda_v) + \frac{1}{2\triangle J+1}\sum_{v=j-\triangle J}^{j+\triangle J} b(i,v). \quad (4.12)$$

We state that due to spectral redundancy, the statistics of the irradiance measured by a particular band are approximately equal to the statistics of the neighboring spectral bands. Hence, $m_X(i,\lambda_j) = m_X(i,\lambda_v)$ for $j-\triangle J \leq v \leq j+\triangle J$, then

$$\overline{m}_Y(i,\lambda_j) = m_X(i,\lambda_j)\frac{1}{2\triangle J+1}\sum_{v=j-\triangle J}^{j+\triangle J} r(\lambda_v)a(i,v) + \frac{1}{2\triangle J+1}\sum_{v=j-\triangle J}^{j+\triangle J} b(i,v) \quad (4.13)$$

$$= m_X(i,\lambda_j)m_{ra}(i) + m_b(i), \quad (4.14)$$

where $m_{ra}(i)$ and $m_b(i)$ represent the spectral average values of the multiplicative and additive terms, respectively. Therefore, we obtain

$$m_X(i,\lambda_j) = \frac{\overline{m}_Y(i,\lambda_j) - m_b(i)}{m_{ra}(i)}. \quad (4.15)$$

By developing Eq. (4.6), we have for the variance:

$$\overline{\sigma^2}_Y(i,\lambda_j) = \frac{1}{2\triangle J+1}\sum_{v=j-\triangle J}^{j+\triangle J}\sigma^2_Y(i,\lambda_j)$$

$$= \sigma^2_X(i,\lambda_j)\frac{1}{2\triangle J+1}\sum_{v=j-\triangle J}^{j+\triangle J}\left[r(\lambda_v)a(i,v)\right]^2 = \sigma^2_X(i,\lambda_j)m_{[ra]^2}(i), \quad (4.16)$$

where $m_{[ra]^2}(i)$ is the average value of the square multiplicative terms. Finally, we have:

$$\sigma^2_X(i,\lambda_j) = \frac{\overline{\sigma^2}_Y(i,\lambda_j)}{m_{[ra]^2}(i)}. \quad (4.17)$$

Finally, let us consider the special case where both the spectral irradiance and the noise parameters are highly correlated in the spectral domain. We have $a(i,j) = a(i)$ and $b(i,j) = b(i)$. Recalling Eq. (4.13) and Eq. (4.16) the following result is obtained

$$\overline{m}_Y(i) = m_X(i,\lambda_j)a(i)\frac{1}{2\triangle J+1}\sum_{v=j-\triangle J}^{j+\triangle J} r(\lambda_j) + b(i)\frac{1}{2\triangle J+1}\sum_{v=j-\triangle J}^{j+\triangle J} 1 \quad (4.18)$$

$$= m_X(i,\lambda_j)a(i)m_r + b(i) \quad (4.19)$$

$$\overline{\sigma}_Y(i,\lambda_j) = \sigma_X(i,\lambda_j)a^2(i,v)\frac{1}{2\triangle J+1}\sum_{v=j-\triangle J}^{j+\triangle J} r^2(\lambda_v) \tag{4.20}$$

$$= \sigma_X^2(i,\lambda_j)a^2(i)m_{r^2}(i). \tag{4.21}$$

It is clear that the parameters defining the striping noise have been mitigated by using the spectral redundancy concept, hence, a single spectral approach can be followed when dealing with a highly correlated noise pattern, but again, the knowledge of the noise structure can be used otherwise.

4.3 Breaking the Spectral Redundancy Assumption and its Effect on the Spectral Resolution

It was mentioned in this thesis that we take advantage of the high spectral resolution provided by a PBHC by assuming spectral redundancy over the hypercube for later use in SNC algorithms. When selecting a spectral subset size that satisfies the spectral redundancy assumption, the SNC process does not reduce the capacity to distinguish spectral information between bands. Kumar *et. al* states that the combination of spectral bandpass and sampling interval determines the spectral resolution of the sensor which, in turn, dictates the spectral discrimination [52]. Based on the sampling theorem and a deconvolution process, Kumar *et. al* effectively extracts 17 non-overlapping bands from 64 bands. These bands exhibit spectral redundancy due to oversampling and crosstalk, therefore, the ability to discriminate spectral information is not affected by averaging redundant spectral data. On the contrary, when the spectral subset size violates a redundancy assumption, a sub-sampling or filtering process can lead to a reduction in spectral resolution over the hypercube.

In general, the loss in resolution is a well known adverse effect produced when low-pass filters are applied in the spatial and/or spectral domain; however, many efforts have been devoted to reduce this undesired effect in the spatial domain [53–55] but only few works have tackled the loss in spectral resolution. Peng *et al.* presented in [23] an extension of the bilateral filter (BF) algorithm introduced by Tomasi and Manduchi [22]. Originally, for a pixel to influence another pixel, it should occupy a nearby spatial location and have a similar intensity value. Hence, the

BF takes a weighted sum of the pixels in a local neighborhood, where the weights depend on both the spatial distance and the intensity differences (range). Tomasi and Manduchi defined two functions to calculate such distances, the closeness function (F_s) and similarity function (F_r) for the spatial and intensity domain, respectively. This filtering scheme is defined as follow:

$$\overline{X}(i,\lambda_j) = \frac{\sum_{u=i-\triangle I}^{i+\triangle I}\sum_{v=j-\triangle J}^{j+\triangle J} \hat{X}(u,v)F_s(u,v,i,\lambda_j)F_r(\hat{X}(u,v),\hat{X}(i,\lambda_j))}{\sum_{u=i-\triangle I}^{i+\triangle I}\sum_{v=j-\triangle J}^{j+\triangle J} F_s(u,v,i,\lambda_j)F_r(\hat{X}(u,v),\hat{X}(i,\lambda_j))}. \tag{4.22}$$

Peng *et al.* proposes to measure the intensity differences in each spectral band, separately, for the design of one filter (F_r) applied in each band. This procedure is useful when images are to be merged, as in multispectral RGB images, but not when the objective is to maintain the spectral resolution during a SNC process. Therefore, we redefine the bilateral algorithm in order to relax the spectral redundancy assumption when using a large spectral subset of bands during the SNC.

Above all, we have to take certain considerations when redefining this filter over the hyperspectral model. Therefore, F_s will be defined as a uniform spatio-spectral filter equal to that implemented in Eq. (4.1), giving the same weight value to each pixel located in the spatio-spectral neighborhood. In this regard, it makes no sense to measure the similarity of the intensity values per band (as presented by Peng *et al.*), since the closeness function now weighs pixels in a neighborhood defined in the spatial and the spectral domain. Thus, the similarity function has to measure the intensities in a central band with respect to its neighboring bands, that is, the spectral intensity between the pixel in the i spatial location at λ_j spectral band and the rest of the pixels in the spatio-spectral neighborhood. In Eq. (4.23), we define F_r as a Gaussian spatio-spectral filter:

$$F_r(\hat{X}(u,v),\hat{X}(i,\lambda_j)) = e^{-\frac{(\hat{X}(u,v)-\hat{X}(i,\lambda_j))^2}{2\sigma_r^2}}. \tag{4.23}$$

The parameter σ_r defines the range of spectral intensity values that are considered as "nearby" values. As σ_r increases, the filter will give the same weight value to each pixel located in the neighborhood, reverting to the traditional BF scheme.

With this new spatio-spectral BF at hand, we integrate this filtering scheme into the NN algorithm presented in Section 4.1. In particular, we intend to enhance the estimation of the multidimensional target value ($\overline{X}(i,\lambda_j,k)$) proposed in Eq. (4.1), eliminating any high spectral difference from the calculation. Then, the multidimensional target value is calculated as follows

$$\overline{X}(i,\lambda_j) = \frac{\sum_{u=i-\triangle I}^{i+\triangle I}\sum_{v=j-\triangle J}^{j+\triangle J}\hat{X}(u,v)e^{-\frac{(\hat{X}(u,v)-\hat{X}(i,\lambda_j))^2}{2\sigma_r^2}}}{\sum_{u=i-\triangle I}^{i+\triangle I}\sum_{v=j-\triangle J}^{j+\triangle J}e^{-\frac{(\hat{X}(u,v)-\hat{X}(i,\lambda_j))^2}{2\sigma_r^2}}}. \tag{4.24}$$

The rest of the estimation process conducted by the multidimentional NN algorithm remains without modification.

4.4 Summary

The spectral redundant information captured from the target scene has been successfully integrated into the multidimensional SNC algorithms. Further, a mathematical analysis is made on the noise spectral structure and its effect on noise compensation. In this sense, Eqs. (4.10), (4.14) and (4.16) prove that the SN parameters are being mitigated through the proposed multidimensional approach. On the other hand, Eqs. (4.11), (4.19) and (4.21) shows that a high spectral correlation on the SN parameters diminish the additional information provided by spectral bands. Nevertheless, this only occurs due to the spectral redundancy previously assumed. If both, a high correlation in the SN parameters and the spectral redundancy are satisfied in the scene, the information that provides a set of neighboring spectral images will be equivalent to that of a single spectral image.

Finally, by considering the spectral variations from the scene, the BF modification has the potential to be an effective tool for relaxing the condition of spectral redundancy in the acquired data. To study this modification, the next chapter include an experimental section that compare the spectral signature resulting from the proposed multidimensional algorithms.

Chapter 5

Experimental Results

In this chapter, the strength and applicability of the proposed multidimensional SNC algorithms are tested using raw hyperspectral data. We have used the setup described in Chapter 3 (see Fig. 3.1) and have acquired different target scenes with the VIS and NIR hyperspectral cameras. For the VIS camera, two hypercubes were collected from the covers of IEEE Signal Processing Magazine. Hypercube 1 contains images with a high variation of tones and colors in the VIS spectral range, while Hypercube 2 contains images with abrupt changes in intensity in order to test how the estimated SN parameters are affected by these rapid changes in the spatial information. Also, the hypercubes CHRIS_YU_120916_EA04_41 and CHRIS_WY_060821_7299_41 acquired using the Earth-observing CHRIS/PROBA CCD sensor were also used. Data in such hypercubes contain different landmarks captured from space. CHRIS_YU_120916_EA04_41 corresponds to the Yasuni National Park, Ecuador and CHRIS_WY_060821_7299_41 corresponds to Redcliff, Canada. Both scenes were selected because their SN patterns have a high contrast against the background information. It must be mentioned that the multidimensional NN SNC algorithm depends on the image-degradation model. Thus, in the experiments conducted in this thesis two models were considered. The first model, labeled as "Model 1," follows the approach in [20] (*cf.* Eq. (2)) and disregards the overall spectral response of the PBHC, that is, $r(\lambda_j) = 1$ for all wavelengths. The second model is the one presented in (2.1) and was labeled as "Model 2.". We have compensated for both the gain and offset parameters, and the performance of the SNC algorithms is evaluated using quality metrics. Moreover, a noise structure analysis is developed

together with a study of the SNC effects on the spectral resolution when the spectral redundancy assumption is violated.

5.1 Striping Noise Performance Metrics

In this section, the four metrics used to compare the SNC performance are presented. The first metric is the root mean squared error (RMSE) between the reference image $\mathbf{X}_{\text{ref}}(\lambda_j)$ and the SN compensated image $\hat{\mathbf{X}}(\lambda_j)$, at wavelength λ_j:

$$\mathbf{RMSE}(\lambda_j) = \Big(\frac{1}{PS}\sum_{i=1}^{P}\sum_{k=1}^{S}(X_{\text{ref}}(i,\lambda_j,k) - \hat{X}(i,\lambda_j,k))^2\Big)^{\frac{1}{2}}, \tag{5.1}$$

where $\mathbf{X}_{\text{ref}}(\lambda_j) = \big(X_{\text{ref}}(i,\lambda_j,l)\big)_{P\times S}$ and $\hat{\mathbf{X}}(\lambda_j) = \big(\hat{X}(i,\lambda_j,l)\big)_{P\times S}$. The reference image is obtained, whenever possible, by means of a laboratory calibration procedure such as the two-point calibration method in [20]. Note that since the RMSE is highly sensitive to bias estimation errors, SN compensated images have been rescaled to the same contrast and brightness as the original corrupted image for valid comparisons.

The second metric is the noise reduction index (NR) and measures the effectiveness of a SNC algorithm. The NR index calculates, at a given wavelength, the ratio between the noise power of the raw and the SN compensated images [12]. The NR index is mathematically defined as:

$$NR(\lambda_j) = \frac{\sum_{u\in U} P_{\bar{Y}}(u,\lambda_j)}{\sum_{u\in U} P_{\bar{\hat{X}}}(u,\lambda_j)}, \tag{5.2}$$

where the $P_{\bar{Y}}(u,\lambda_j)$ and $P_{\bar{\hat{X}}}(u,\lambda_j)$ are, respectively, the magnitude power spectrum, at the frequency component u and wavelength λ_j, of the time-averaged cross-track profile of the raw and the SN compensated images. More precisely, $P_Y(u,\lambda_j) = |\text{DFT}\{\bar{Y}(i,\lambda_j)\}|$ with $\bar{Y}(i,\lambda_j) = S^{-1}\sum_{k=1}^{S} Y(i,\lambda_j,k)$, $P_{\bar{\hat{X}}}(u,\lambda_j) = |\text{DFT}\{\bar{\hat{X}}(i,\lambda_j)\}|$ with $\bar{\hat{X}}(i,\lambda_j) = S^{-1}\sum_{k=1}^{S}\hat{X}(i,\lambda_j,k)$, and $\text{DFT}\{\cdot\}$ is the discrete Fourier transform. In (5.2), the set U represents those frequencies where the SN components are concentrated [12]. A reduction in the SN power is obtained when the NR index is larger than one.

The third metric used here is the improvement factor (IF) and quantifies the

impact of the SNC algorithm on the radiometric quality of the image [56]. This index is defined as:

$$IF(\lambda_j) = 10\log_{10}\left(\frac{\sum_{i=1}^{P}(\bar{Y}(i,\lambda_j) - \bar{\hat{X}}(i,\lambda_j)\otimes f)^2}{\sum_{i=1}^{P}(\bar{\hat{X}}(i,\lambda_j) - \bar{\hat{X}}(i,\lambda_j)\otimes f)^2}\right), \tag{5.3}$$

where f is a 5×1 averaging low-pass filter and the symbol $\otimes$ represents the discrete convolution. The quantity $\bar{\hat{X}}(i,\lambda_j)\otimes f$ is termed in [56] as the noise free cross-track profile, and represents an estimate of the actual signal. Thus, a higher IF value indicates an improvement on the radiometric quality of the compensated image.

The last metric used in this paper is a modified version of the roughness index in [57]. This index is used in NUC of infrared images due to its ability to quantify the amount of grid-like noise in infrared images [57]. Unlike the original metric, the SN roughness index, ρ_{SN}, quantifies the amount of SN in an image, at each wavelength, and is defined as:

$$\rho_{SN}(\lambda_j) = \frac{||\mathbf{h}\otimes\hat{\mathbf{X}}(\lambda_j)||}{||\hat{\mathbf{X}}(\lambda_j)||}, \tag{5.4}$$

where $\mathbf{h}$ is a high-pass filter, $||\cdot||$ is the ℓ^1-norm, and the symbol $\otimes$ represents the discrete 2D convolution. In (5.4), the filter $\mathbf{h}$ is designed to detect the intensity variations in the cross-track direction and is defined as the vector $\mathbf{h} = [-1\ 1]$. Consequently, the SN roughness index measures the spatial frequency components of the noise. From (5.4), it can be observed that ρ_{SN} is a non-negative real number, with $\rho_{SN}(\lambda_j) = 0$ whenever $\hat{\mathbf{X}}(\lambda_j)$ is flat; therefore, the closer ρ_{SN} to zero the better the SNC.

5.2 Multidimensional Striping Noise Compensation Analysis

The initial conditions for the recursive NN SNC algorithm were set to $\hat{g}(i,j,0) = 1$ and $\hat{o}(i,j,0) = 0$ for all the pixels in the array. A total number of $S = 800$ recursions were carried out for each pixel. In addition, to compute the multidimensional target value a spatial neighborhood of $2\Delta I + 1 = 3$ pixels and subsets of $2\Delta J + 1 = \{1, 15, 31, 61, 91, 151, 181\}$ adjacent spectral bands were considered (see Eq. (4.1)).

Also, the learning rates in (4.3) and (4.4) were regarded, for simplicity, as constants and set to $\eta_g(\lambda_j) = 5 \cdot 10^{-10}$ and $\eta_o(\lambda_j) = 5 \cdot 10^{-2}$ for all wavelengths. These values were obtained experimentally by minimizing the RMSE between calibrated and compensated images.

Table 5.1: Hypercube 1: Performance metrics as a function of the number of adjacent spectral bands, for a hyperspectral image at 686 [nm] when the multidimensional NN algorithm was used to compensate for the SN.

		Number of spectral adjacent bands: $2\Delta J + 1$						
Metric	Model	1	15	31	61	91	151	181
RMSE	1	77.68	76.39	76.64	75.18	73.18	71.48	71.51
	2	42.94	38.66	36.78	36.62	37.22	38.88	40.10
NR	1	2.10	2.16	2.14	2.15	2.19	2.30	2.35
	2	5.88	6.84	6.92	6.96	6.96	6.91	6.88
IF	1	25.87	28.63	28.43	28.21	28.47	30.03	30.96
	2	23.52	24.94	25.13	25.18	25.20	25.16	25.15
ρ_{SN}	1	0.0268	0.0266	0.0267	0.0267	0.0265	0.0259	0.0256
	2	0.0176	0.0162	0.0162	0.0160	0.0161	0.0162	0.0162

Tables 5.1 and 5.2 list the performance results of the multidimensional NN SNC algorithm as a function of the number of adjacent spectral bands. Results for all metrics show an increase in their values as the number spectral bands does, which represents an effective compensation on the SN parameters for a spectral image. In terms of the RMSE, results show that Model 2 outperforms Model 1, even in the unidimensional case ($2\Delta J + 1 = 1$). In particular, the lowest values achieved by the RMSE was 36.62 (respectively, 23.04) when 61 (respectively, 181) adjacent spectral bands of Hypercube 1 (respectively, Hypercube 2) were used to compensate for the SN. Similar results for Model 2 were observed in terms of the NR metric for both hypercubes. More precisely, the NR factor was equal to 6.96 (respectively, 10.22) when 61 (respectively, 181) adjacent spectral bands were used during the SNC process of Hypercube 1 (respectively, Hypercube 2). In terms of the IF metric, Model 2 outperforms Model 1 only in the case of the Hypercube 2 data set, also when 181 spectral bands are used during the SNC process. However, for Hypercube 1, Model 1 achieves the best results but both models do exhibit an overall improvement on the compensated images. This can be explained by analyzing the IF mechanics, which measures the radiometric accuracy on the compensated images. In this sense, the

use of highly variable spectral data during the SNC modified the overall radiometric response for the spectral image.

Table 5.2: Hypercube 2: Performance metrics as a function of the number of adjacent spectral bands, for a hyperspectral image at 728 [nm] when the multidimensional NN algorithm was used to compensate for the SN.

		Number of spectral adjacent bands: $2\Delta J + 1$						
Metric	Model	1	15	31	61	91	151	181
RMSE	1	88.31	89.66	78.99	68.26	64.60	62.25	61.44
	2	32.49	32.09	31.06	28.15	26.56	23.99	23.04
NR	1	3.09	2.92	3.00	3.19	3.28	3.31	3.31
	2	11.33	11.56	11.19	10.76	10.45	10.21	10.22
IF	1	24.30	24.88	25.68	27.23	28.01	28.75	28.92
	2	34.37	34.79	34.85	35.17	35.50	36.05	36.28
ρ_{SN}	1	0.0225	0.0229	0.0226	0.0220	0.0216	0.0214	0.0214
	2	0.0121	0.0119	0.0121	0.0123	0.0124	0.0125	0.0125

For the SN roughness metric, all the values are close to zero meaning that both hypercubes were effectively compensated for the SN. Also, it can be observed that the ρ_{SN} index remains almost constant when more than one spectral band is used to compensate for the SN. From a conceptual point of view, the ρ_{SN} measures the amount of high frequency components that are presents in the image and, by obtaining similar value after the SNC when increasing the spectral bands subset, it is safe to assume that the algorithm does not reduce the spatial details of the scene. It should be noted that a ρ_{SN} value closer to zero could indicate that the algorithm is malfunctioning, removing frequency components of the scene, producing a flat image. Hence, a visual inspection of the compensated image is required for a better interpretation of the ρ_{SN} metric, which will be presented later in this Section.

Tables 5.3 and 5.4 list the values of the performance metrics for hyperspectral images, at different spectral bands, when 61 adjacent spectral bands were used to compensate for the noise. The results achieved by the image quality metrics show that all the spectral images were successfully compensated for the SN. From Table 5.3, the best results were achieved for the hyperspectral image at 707 [nm]. When Model 2 was used, the RMSE was equal to 34.15 while the NR factor was 7.68. From Table 5.4, the best results were obtained for the hyperspectral image at 748 [nm], with an RMSE of 28.05 and an NR factor of 12.11. It is worth mentioning that estimation

procedure for both Tables 5.3 and 5.4 was made considering the same learning rate at each spectral band. It should be noted that the SNC could be improved by selecting a different learning rate for each spectral image according to the variability of the acquired spatio-spectral information.

Table 5.3: Hypercube 1: Performance metrics for some hyperspectral images, when 61 spectral bands were used by the multidimensional NN algorithm to compensate for the SN.

		Central wavelength [nm]				
Metric	Model	644	665	686	707	728
RMSE	1	72.21	90.16	75.18	121.15	99.76
	2	31.14	32.92	36.62	34.15	36.97
NR	1	2.18	2.01	2.15	1.93	1.92
	2	6.68	6.74	6.96	7.68	7.10
IF	1	28.75	29.26	28.21	28.42	28.25
	2	25.25	25.38	25.18	25.99	24.83
ρ_{SN}	1	0.0264	0.0271	0.0267	0.0277	0.0275
	2	0.0163	0.0161	0.0160	0.0154	0.0157

Table 5.4: Hypercube 2: Performance metrics for some hyperspectral images, when 61 spectral bands were used by the multidimensional NN algorithm to compensate for the SN.

		Central wavelength [nm]				
Metric	Model	686	707	728	748	769
RMSE	1	63.04	86.27	68.26	77.03	94.38
	2	34.35	28.11	28.15	28.05	45.65
NR	1	3.59	3.10	3.19	3.38	3.37
	2	11.03	11.45	10.76	12.11	11.86
IF	1	26.00	27.34	27.23	26.95	25.13
	2	33.72	36.46	35.17	36.25	35.19
ρ_{SN}	1	0.0221	0.0221	0.0220	0.0209	0.0172
	2	0.0129	0.0118	0.0123	0.0114	0.0094

Proceeding with the MM SNC algorithm. To initialize the recursions (4.5) and (4.6), the sample mean and the sample standard deviation, in the along-track direction, must be calculated using $2\Delta J+1$ adjacent spectral bands. As in the case of the multidimensional NN algorithm, subsets containing $2\Delta J+1 = \{1, 15, 31, 61, 91, 151, 181\}$

spectral bands were considered. It must be noted that, unlike the NN algorithm, the multidimensional MM SNC algorithm does not depend on the overall spectral response of the PBHC due to such terms that are canceled out in (3.1). Consequently, the SNC properties of this algorithm hold for both Model 1 and Model 2.

Tables 5.5 and 5.6 list the performance metrics achieved by the MM SNC algorithm. From the tables, the best values were obtained when 61 adjacent spectral bands were used during the image destriping process. For Hypercube 1, the RMSE was 50.23, the NR factor was 1.90, and the IF index was 12.97 while, for Hypercube 2, the RMSE was 62.64, the NR factor was 2.37, and the IF index was 12.25. As in the case of the NN algorithm, the roughness metric was close to zero in all cases and remained almost constant when more than one spectral band was used to compensate for the SN. The discarded value from the IF in Tables 5.5 and 5.6, when the unidimentional case is considered, is due to the condition imposed by the MM algorithm and how the IF metric is calculated. That is, the original MM algorithm imposes that the temporal mean calculated in the along-track direction needs to be the same for all the detectors in that spectral band, generating a compensated image with a constant cross-track profile. Hence, when the IF is applied, the low-pass filter used for estimating the noise free cross-track profile produces the same constant value. Finally, the difference between the estimated cross-track and noise free profiles is close to zero in the denominator, generating an abnormal large value for the IF metric.

Table 5.5: Hypercube 1: Performance metrics as a function of the number of adjacent spectral bands, for a hyperspectral image at 686 [nm], when the multidimensional MM algorithm was used to compensate for the SN.

		Number of spectral adjacent bands: $2\Delta J + 1$						
Metric	Model	1	15	31	61	91	151	181
RMSE	2	92.74	60.18	52.22	50.23	50.82	51.55	52.38
NR	2	1.57	1.76	1.84	1.90	1.90	1.89	1.88
IF	2	–	9.47	11.47	12.97	13.15	13.11	13.02
ρ_{SN}	2	0.0311	0.0375	0.0345	0.0326	0.0325	0.0326	0.0327

As in Tables 5.3 and 5.4, raw hyperspectral images at different spectral bands were compensated for SN using a fixed number of 61 adjacent spectral bands. Tables 5.7 and 5.8 present the results achieved by the multidimensional MM algorithm for the different quality metrics. From Table 5.7, the best result was achieved for the

Table 5.6: Hypercube 2: Performance metrics as a function of the number of adjacent spectral bands, for a hyperspectral image at 728 [nm], when the multidimensional MM algorithm was used to compensate for the SN.

		Number of spectral adjacent bands: $2\Delta J + 1$						
Metric	Model	1	15	31	61	91	151	181
RMSE	2	66.44	64.55	63.42	62.64	65.03	65.34	67.82
NR	2	2.22	2.21	2.33	2.37	2.41	2.42	2.44
IF	2	–	10.28	11.72	12.25	12.37	12.84	12.87
ρ_{SN}	2	0.0264	0.0355	0.0326	0.0317	0.0315	0.0311	0.0311

hyperspectral image at 644 [nm], where the RMSE was 49.77, the NR factor was 1.84, and the IF was 11.91. Similarly, from Table 5.8, the SN compensated hyperspectral image at 686 [nm] scored a RMSE of 50.64, a NR factor of 2.45, and an IF of 12.43.

Table 5.7: Hypercube 1: Performance metrics for some hyperspectral images, when 61 spectral bands were used by the multidimensional MM algorithm to compensate for the SN.

		Central wavelength [nm]				
Metric	Model	644	665	686	707	728
RMSE	2	49.77	60.63	50.22	74.61	60.91
NR	2	1.84	1.64	1.90	1.56	1.76
IF	2	11.91	11.10	12.97	11.21	12.45
ρ_{SN}	2	0.0346	0.0358	0.0326	0.0369	0.0333

Table 5.8: Hypercube 2: Performance metrics for some hyperspectral images, when 61 spectral bands were used by the multidimensional MM algorithm to compensate for the SN.

		Central wavelength [nm]				
Metric	Model	686	707	728	748	769
RMSE	2	50.64	71.01	62.64	72.64	87.54
NR	2	2.45	2.27	2.37	2.47	1.88
IF	2	12.43	11.66	12.25	12.18	10.49
ρ_{SN}	2	0.0318	0.0342	0.0317	0.0303	0.0267

A comparison between raw hyperspectral images and their corresponding SN compensated versions is depicted in Figs. 5.1 and 5.2 for the case of Model 2. A simple naked-eye inspection shows that the multidimensional NN and MM algorithms are

indeed efficient in eliminating the SN, and moreover, they provide better results than those obtained using the unidimensional SNC algorithms.

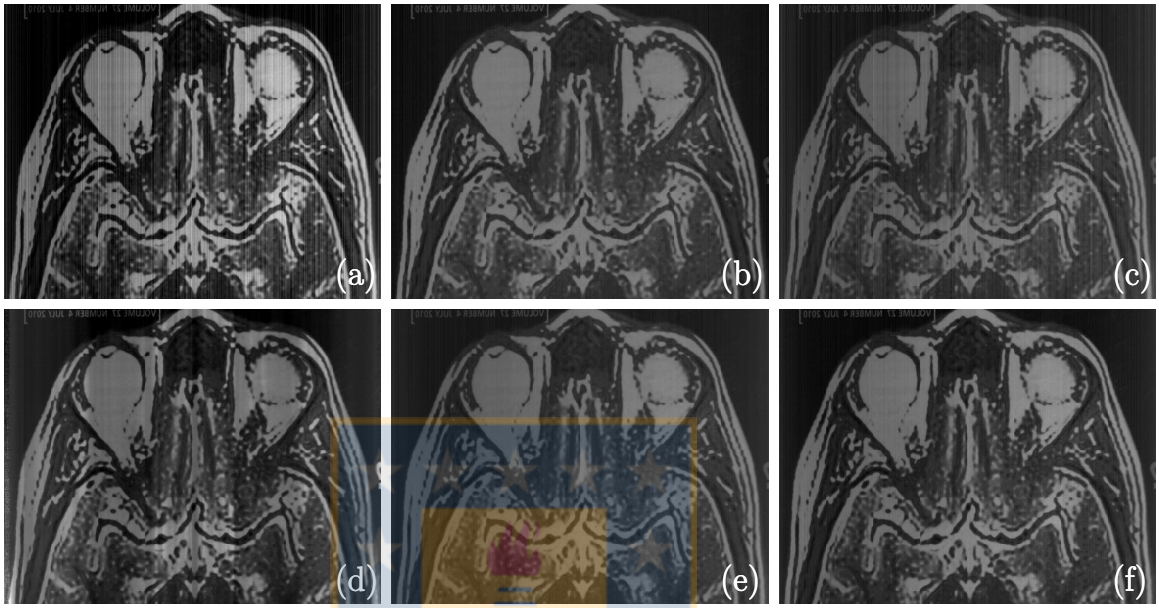

Figure 5.1: Hypercube 1: Sample image at 686 [nm] and compensated using Model 2. (a) Raw image; and (b) reference image. SN compensated images obtained using the unidimensional: (c) NN algorithm; and (d) MM algorithm. SN compensated images obtained using the multidimensional: (e) NN algorithm; and (f) MM algorithm. In the latter two cases algorithms exploited information from 61 adjacent spectral bands.

A closer examination to Figs. 5.1(e) and 5.1(f) shows regions with fewer vertical artifacts than those appearing in Figs. 5.1(c) and 5.1(d). This shows that the SN compensated images rendered by the multidimensional algorithms have smoother intensity transitions between spatial pixels. It should be noted that these artefacts are produced by a poor estimation of the gain and offset parameters [57]. That is, when compensating for a particular spectral band, the reassembled spectral image carries the estimation error along the scanning direction, superimposing spatial information unrelated to the original image. The most compelling evidence about the excellent performance of the multidimensional MM algorithm images can be observed in Fig. 5.2. Note that the words, and more precisely, the letters in Fig. 5.2(f) are smoother, less blurry, and show fewer vertical artifacts than those in Fig. 5.2(d).

As an overall comparison between the two multidimensional SNC algorithms proposed here, results show that the NN algorithm slightly outperforms the MM algo-

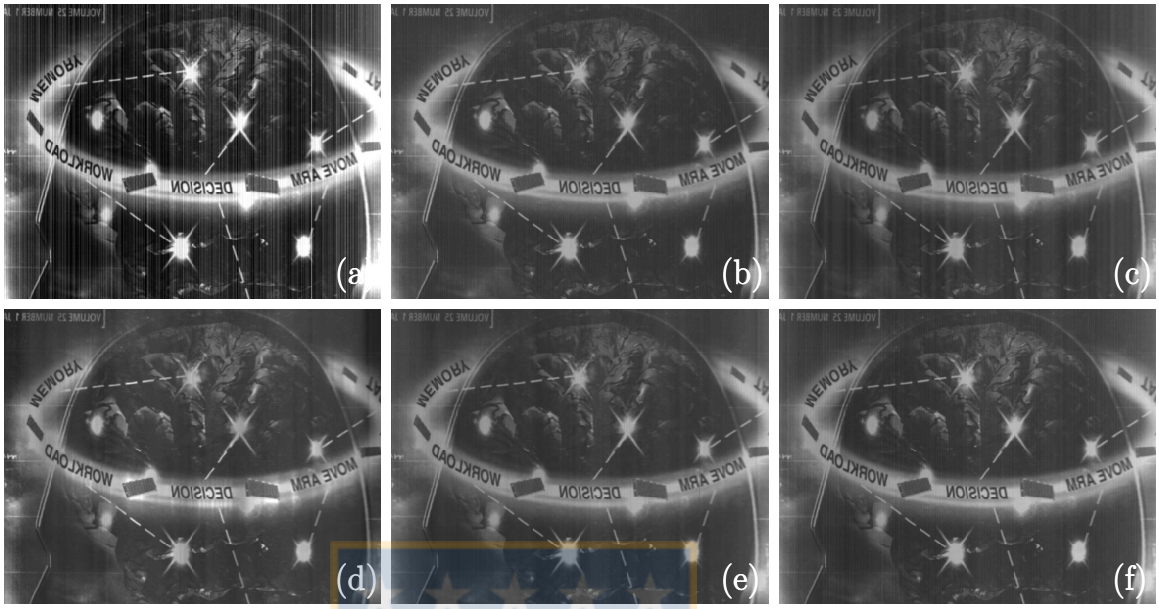

Figure 5.2: Hypercube 2: Sample image at 728 [nm] and compensated using Model 2. (a) Raw image; and (b) reference image. SN compensated images obtained using the unidimensional: (c) NN algorithm; and (d) MM algorithm. SN compensated images obtained using the multidimensional: (e) NN algorithm; and (f) MM algorithm. In the latter two cases algorithms exploited information from 61 adjacent spectral bands.

rithm. This difference lies in the estimation method used by each algorithm. While the efficiency of the MM algorithm relies on the accuracy of the estimated statistics of the whole scene, the NN algorithm uses a learning rate to adjust each iteration step to reach its global minimum. This adaptive feature results in lesser artifacts in the SN compensated images than in the case of the MM algorithm, even when there is little variability in the data [58].

5.2.1 Striping Noise Compensation over Correlated Noise Parameters

As a proof of concepts, we conducted an experimental analysis on the SNC algorithms when a highly correlated noise between bands affect the hypercube, which will verify what was demonstrated in Section 4.2. It should be remarked that the SNC algorithms are expected to perform poorly due to the violation of this assumption. The algorithms are tested using raw hyperspectral data acquired with the NIR hyperspectral camera. As in Chapter 3.1, the FPA of the NIR camera is affected by

a stripe-like pattern due to its readout architecture (PPS). Furthermore, the size of the corrupted hypercube is equal to 320 × 236 × 500 in the spatial, spectral and temporal domain, respectively.

Table 5.9: Performance metrics as a function of the number of adjacent spectral bands, for a hyperspectral image at 1332 [nm], when the multidimensional SNC algorithms were used to compensate for the SN.

			Number of spectral adjacent bands: $2\Delta J + 1$				
Metric	Method	Model	31	61	91	151	181
RMSE	NN	1	214.74	209.85	204.67	200.77	200.69
	NN	2	105.27	105.61	105.99	107.15	107.56
	MM	2	213.52	216.57	219.29	223.29	225.34
NR	NN	1	1.05	1.06	1.06	1.06	1.06
	NN	2	1.70	1.69	1.69	1.67	1.67
	MM	2	1.04	1.04	1.04	1.03	1.02
IF	NN	1	1.12	1.23	1.36	1.43	1.42
	NN	2	11.32	11.21	11.13	10.86	10.76
	MM	2	1.00	0.84	0.77	0.58	0.49
ρ_{SN}	NN	1	0.0790	0.0785	0.0779	0.0780	0.0781
	NN	2	0.0415	0.0416	0.0417	0.0421	0.0427
	MM	2	0.0798	0.0812	0.0818	0.0831	0.0839

The performance metrics for the compensated image taken at 1332 [nm], considering spectral subsets of different sizes, are presented in Table 5.9. It can be observed, all the quality metrics of the processed images are very similar, independent of the number of bands considered in the SNC process. For the sake of clarity, the following results are presented in terms of its average. The NN algorithm using Model 1 achieves an average RMSE of 206.14, with a NR of 1.06 and IF of 1.31. For the MM algorithm, the results are similar to the previous, scoring an average RMSE of 219.60, with a NR of 1.31 and IF of 0.74. This type of behavior is expected due to the results obtained in Section 4.2. However, the NN algorithm using Model 2 obtain an average RMSE of 106.32, a NR equal to 1.68 and a IF of 11.06. The results are remarkably good for this experiment, not for the compensation of SN parameters, but for the use of Model 2. This Model separates the system spectral response from the multiplicative noise term, weighing the spectral intensities during the SNC. Therefore, the variability of the spectral information is lowered, achieving a more accurate intensity distribution for the spectral image than by assuming a uniform system response.

It is worth mentioning that, when using the extended MM algorithm with a subset size $\Delta J = 0$, the algorithm works like the traditional case without contaminating the statistics of the selected spectral band with the noise statistics of neighbouring bands.

Moreover, the reassembled images obtained after the SNC process, considering 61 spectral bands, are presented in Fig. 5.3. As expected, when comparing the raw image (Fig. 5.3.a) with its compensated versions (Figs. 5.3.b-d), it is clear that the noise pattern affecting the spectral image was not reduced.

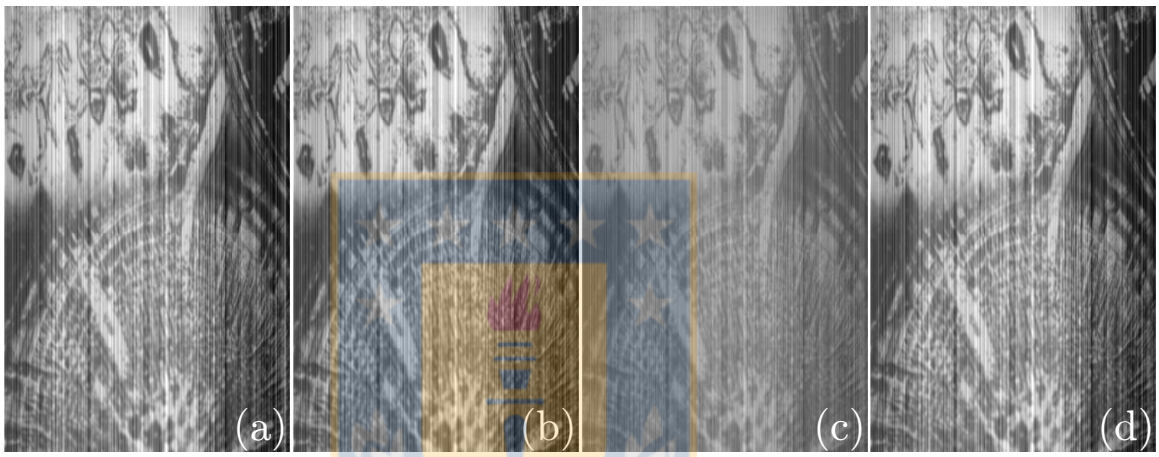

Figure 5.3: Sample image at 1132 [nm]. (a) Raw image. SN compensated images obtained using the multidimensional: (b) NN algorithm with Model 1; (c)NN algorithm with Model 2; and (d) MM algorithm using Model 1. In the latter three cases algorithms exploited information from 61 adjacent spectral bands.

Additionally, we have compensated raw data acquired from the Earth-observing CHRIS/PROBA CCD sensor, where this type of sensor is an example of a PBHC exhibiting highly correlated SN parameters. That is, the CCD offer high quantum efficiency due to the use of a PPS readout architecture, which prevents limiting the effective area with integrated amplifiers per detector but generating a highly correlated pattern between rows [8].

The selected data consists in two hypercubes, whose dimensions are 66 spectral bands, with a spatial resolution of 336 pixel and 320 samples taken during the scanning procedure. Hypercubes CHRIS_YU_120916_EA04_41 and CHRIS_WY_060821_7299_41 were compensated for SN using the multidimensional NN and MM algorithms considering a subset of 25 adjacent spectral bands. Due to the overall spectral response of the sensor is unknown, the image-degration model used in the evaluations corresponds

to Model 1.

Performance results achieved by the algorithms are listed in Table 5.10. For comparison, the roughness index of the raw hyperspectral images are, respectively, 3.66 and 2.93 for the CHRIS_YU_120916_EA04_41 and CHRIS_WY_0608 21_7299_41 hypercubes. From the tables, it becomes clear that the MM algorithm does not compensate for the SN because, for instance, in the case of CHRIS_YU_120916_EA 04_41 the algorithm scored an IF of 0.32 (no improvement) and a roughness index of 3.62, which is very close to the roughness index of the raw image. Further, the same behavior can be observed for Hypercube CHRIS_WY_060821_7299_41 .

Table 5.10: Performance metrics for the CHRIS/PROBA data set. Hyperspectral image in channel 20 was compensated for the SN using 25 adjacent spectral bands and the multidimensional NN and MM algorithms.

	CHRIS_YU_120916_EA04_41		CHRIS_WY_060821_7299_41	
Metric	NN	MM	NN	MM
NR	1.03	1.02	1.05	1.01
IF	17.61	0.32	20.29	0.72
ρ_{SN}	0.0316	0.0362	0.0207	0.0292

Unlike the MM algorithm, Table 5.10 shows also that the multidimensional NN algorithm yields some reduction in the SN, regardless of using spectral information corrupted by the same SN pattern. For this algorithm, the IF achieved was 17.61 (correspondingly, 20.29) for Hypercube CHRIS_YU_120916_EA04_41 (correspondingly, Hypercube CHRIS_WY_060821_7299_41), with a roughness index of 0.0316 (correspondingly, 0.0207). It should be noted that the relative large IF value obtained with the NN compensated images is due to the IF mechanics. That is, the IF assumes that a good representation of a noise free profile is obtained applying an averaging low-pass filter over the estimated signal. When the NN algorithm is applied over a data set with correlated SN parameters, the SNC is performed only by the averaging process in the spatial dimension. This results in a cross-track profile similar to that assumed by the metric, reducing the error and increasing the IF value.

From Fig. 5.3 and 5.4, it can be observed that some SN pattern still remains on top of the compensated hyperspectral images. As expected, hyperspectral images compensated by means of the multidimensional NN algorithm exhibit lesser SN patterns than those compensated using the MM algorithm. This destriping capability

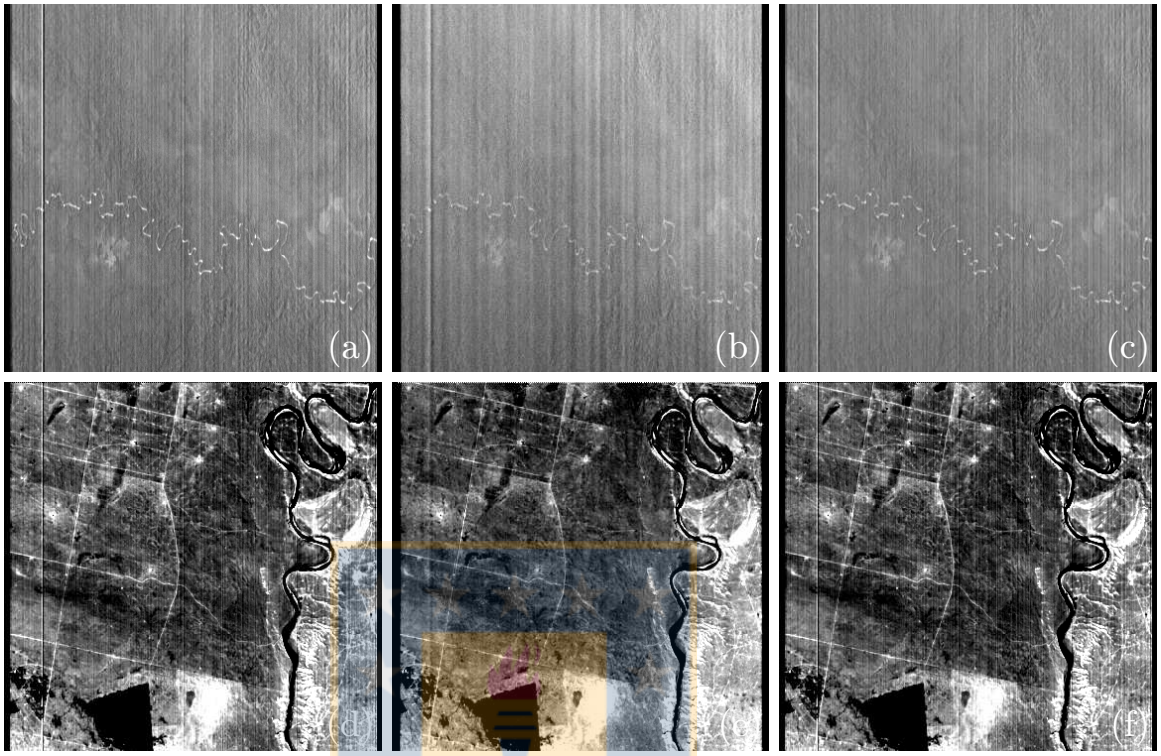

Figure 5.4: Raw satellite images taken with ESA Earth-observing CHRIS/PROBA sensor at channel 20. Hypercube CHRIS_YU_120916_EA04_41: (a) raw hyperspectral image. SN compensated images obtained using the multidimensional: (b) NN algorithm; and (c) MM algorithm. Hypercube CHRIS_WY_060821_7299_41: (d) raw hyperspectral image. SN compensated images obtained using the multidimensional: (e) NN algorithm; and (f) MM algorithm.

in the NN algorithm is attributed to the averaging process, in the spatial dimension, conducted by the algorithm when using a single spectral band. Such compensation does not occur in the MM algorithm because estimates are obtained in a pixel wise fashion in the temporal domain and the spatial information is disregarded.

5.3 Preserving the Spectral Resolution

As mentioned in Chapter 4, the multidimensional SNC process can affect the ability to distinguish spectral information between neighboring bands depending on how the compensation scheme is carried out. In this section, we evaluate the performance of SNC algorithms over the spectral domain when the spectral redundancy assumption

is violated. First, we compare the SNC schemes in term of a specific reassembled image to analyze the level of compensation achieved by each algorithm. Second, we compared the spectral signature obtained when the hypercube is compensated to determine which scheme introduces less modifications over the spectral information. In particular, we are comparing three versions of the multidimensional NN algorithm to reduce the number of parameters to evaluate. The versions of the algorithm are the following:

i The multidimensional NN algorithm based on Model 1 (see Section 4.1).

ii The multidimensional NN algorithm based on Model 2 (see Section 4.1).

iii The multidimensional NN algorithm based on Model 2, including the proposed modification on the target image estimation (see Section 4.3).

Since the modification using the BF scheme for calculating the target value (see Section 4.3) is based on measuring the differences between spectral intensities through a Gaussian function, we have evaluated different values for the filter parameter ($\sigma_r = \{1, 5, 10, 25\}$). Furthermore, when computing the multidimensional target value for the three algorithms, we have employed a spatial subset with $\Delta I = 1$ pixels and a spectral band subset of $2\Delta J + 1 = \{61, 91, 151, 181\}$ pixels. It should be noted that we have considered these subset sizes to push the spectral assumption to the limit. Also, the algorithms are tested over the same hypercubes used in Section 5.2. In the following Tables 5.11 and 5.14, the SNC results obtained under these conditions are in terms of the RMSE and ρ_{SN} metrics.

The RMSE values presented in Table 5.11 indicate that the modification with the BF can achieve equivalent results compared to the multidimensional NN algorithm without modification. The best RMSE value is 36.62 for the NN algorithm using Model 2 and a RMSE of 36.51 when using the BF with $\sigma_r = 10$. In both cases the subset of spectral bands is equal to 61. Further, it is shown that decreasing the σ_r produces RMSE values relatively higher compared to $\sigma_r = 25$. The amount of the spectral information taken into account is limited by the size of the BF and the spectral signature redundancy observed in the selected spectral subset.

In Table 5.12, the ρ_{SN} values confirm the presence of high frequency components after the SNC, denoting the existence of remaining stripe noise and some artifacts

Table 5.11: Hypercube 1: RMSE values as a function of the number of adjacent spectral bands, for a hyperspectral image at 686 [nm], when the multidimensional NN algorithm was used to compensate for the SN.

			Number of spectral adjacent bands: $2\Delta J+1$			
Metric	Model	σ_r	61	91	151	181
NN	1	-	75.18	73.18	71.48	71.51
NN	2	-	36.62	37.22	38.88	40.10
NN :(BF)	2	1	48.45	48.41	48.42	48.43
NN :(BF)	2	5	42.60	42.45	43.86	44.43
NN :(BF)	2	10	36.51	36.80	38.65	39.39
NN :(BF)	2	25	36.94	36.99	38.38	39.31

Table 5.12: Hypercube 1: ρ_{SN} values as a function of the number of adjacent spectral bands, for a hyperspectral image at 686 [nm], when the multidimensional NN algorithm was used to compensate for the SN.

			Number of spectral adjacent bands: $2\Delta J+1$			
Metric	Model	σ_r	61	91	151	181
NN	1		0.0267	0.0265	0.0259	0.0256
NN	2		0.0160	0.0161	0.0162	0.0162
NN :(BF)	2	1	0.0389	0.0389	0.0389	0.0389
NN :(BF)	2	5	0.0272	0.0271	0.0297	0.0308
NN :(BF)	2	10	0.0159	0.0156	0.0176	0.0186
NN :(BF)	2	25	0.0156	0.0157	0.0155	0.0155

produced during the compensation. The best ρ_{SN} values are 0.0160 and 0.0155 for the NN algorithm using Model 2 and for the BF with $\sigma_r = 25$, respectively. It should be remarked that the ρ_{SN} metric has shown similar behavior to that seen with the RMSE metric when different σ_r values are evaluated. Figure 5.5 displays the compensated images, at 686 [nm], when considering 151 adjacent spectral bands.

When comparing the reference image (Fig. 5.5.b) with its compensated versions, it is clear that the best results are obtained with the NN scheme based on Model 2 (Fig. 5.5.d) and the spatio-spectral BF with $\sigma_r = 25$ (Fig. 5.5.f). In particular, the remaining striping noise observed in Fig. 5.5.e is due to the small value of σ_r. Namely, a small standard deviation reduces the range of spectral intensities considered in the spatio-spectral neighbourhood, decreasing the amount of information processed during the noise compensation. However, a small value of σ_r can be beneficial when

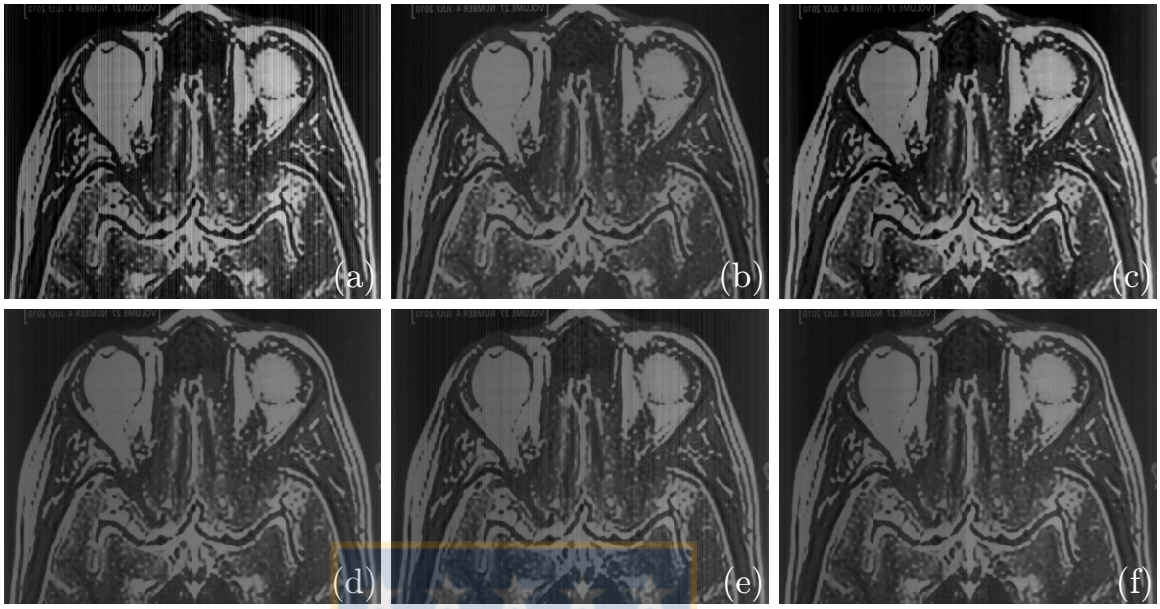

Figure 5.5: Hypercube 1: Sample image at 686 [nm]. (a) Raw image; and (b) reference image. SN compensated images obtained using Model 1 and the: (c) NN algorithm. SN compensated images obtained using Model 2 and the: (d) NN algorithm; (e) NN algorithm with the BF modification and $\sigma_r = 5$; and (f) NN algorithm with the BF modification and $\sigma_r = 25$. The algorithms exploited information from 151 adjacent spectral bands.

facing a scene with a highly variable spectral signature.

Table 5.13: Hypercube 2: RMSE values as a function of the number of adjacent spectral bands, for a hyperspectral image at 728 [nm], when the multidimensional NN algorithm was used to compensate for the SN.

			Number of spectral adjacent bands: $2\Delta J + 1$			
Metric	Model	σ_r	61	91	151	181
NN	1		68.26	64.30	62.25	61.44
NN	2		28.15	26.56	23.99	23.04
NN :(BF)	2	1	40.85	40.83	40.80	40.80
NN :(BF)	2	5	36.39	36.05	35.31	35.53
NN :(BF)	2	10	32.63	31.81	30.64	30.92
NN :(BF)	2	25	28.63	26.46	25.14	24.42

For Hypercube 2, Tables 5.13 and 5.14 display similar results as those obtained using Hypercube 1. In particular, the RMSE values obtained when $\sigma_r = 5$ are remarkably good (35.31 considering 151 adjacent spectral bands), however, they exhibit

a high ρ_{SN} value (0.0227 considering 151 adjacent spectral bands). This ρ value is due to the presence of residual noise in the compensated image.

Table 5.14: Hypercube 2: ρ_{SN} values as a function of the number of adjacent spectral bands, for a hyperspectral image at 728 [nm], when the multidimensional NN algorithm was used to compensate for the SN.

			Number of spectral adjacent bands: $2\Delta J + 1$			
Metric	Model	σ_r	61	91	151	181
NN	1		0.0220	0.0216	0.0214	0.0214
NN	2		0.0123	0.0124	0.0125	0.0125
NN :(BF)	2	1	0.0351	0.0351	0.0350	0.0350
NN :(BF)	2	5	0.0228	0.0231	0.0227	0.0235
NN :(BF)	2	10	0.0140	0.0147	0.0142	0.0146
NN :(BF)	2	25	0.0127	0.0120	0.0119	0.0118

Figure 5.6 displays the compensated images, at 728 [nm], when considering a spectral subset size of 151. As expected, Figs. 5.6.d and 5.6.f exhibit the best compensation when compared to the rest. Further, Fig. 5.6.e shows some remaining striping noise after the compensation, which corroborates the 0.0227 roughness value. However, this image shows a regular background intensity level when compared to Fig. 5.6.c (with less artifacts), which in turn explains the low RMSE value of 35.31.

The following analysis shows the effect produced over the spectral resolution after the hypercube is compensated for the SN. The spectral range under analysis is selected due to the high variation observed in the spectral data. It should be noted that the curves are displayed with a fixed intensity range for comparative purposes.

In Fig. 5.7, it is appreciated that all the spectral curves obtained after the SNC present a shift on the base level with respect to the reference (Fig. 5.7.a). The curves in Figs. 5.7.b and 5.7.c show similarities with respect to the reference spectral curve, but with a noticeable change in the spectral intensities range. Further, the spectral curve observed in Fig. 5.7.e not only shows a similar shape to the reference curve, but also a more accurate intensity estimation. Comparing the shifts in the base level observed in the spectral curves, the results in Fig. 5.7.d and Fig. 5.7.e are closer to the reference curve. This result is consistent with what was expected since the BF weighs differently the information of neighboring bands, discarding the outliers from the estimation.

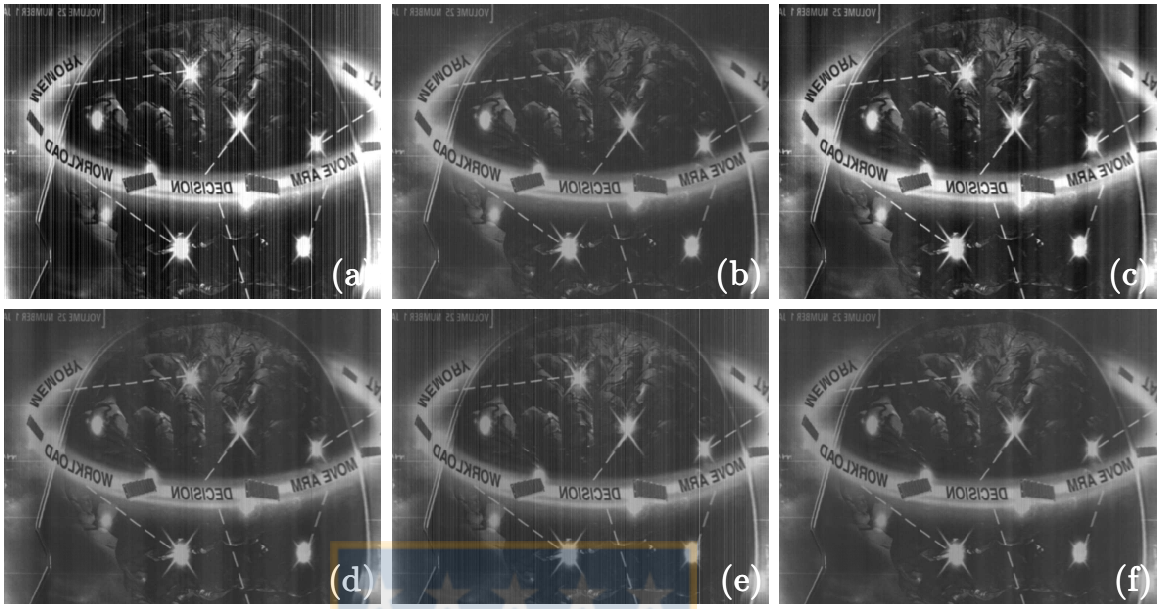

Figure 5.6: Hypercube 2: Sample image at 728 [nm]. (a) Raw image; and (b) reference image. SN compensated images obtained using Model 1 and the: (c) NN algorithm. SN compensated images obtained using Model 2 and the: (d) NN algorithm; (e) NN algorithm with the BF modification and $\sigma_r = 5$; and (f) NN algorithm with the BF modification and $\sigma_r = 25$. The algorithms exploited information from 151 adjacent spectral bands.

As illustrated in Figs. 5.8.b and 5.8.c, the loss of spectral details due to the averaging process performed by each algorithm is more evident than in Fig. 5.7. Further, the Fig. 5.8.d shows that the spectral signature is still affected by noise after the compensation, which is corroborated with the reassembled image observed in Fig. 5.6.e. Nevertheless, the spectral curve presented in Fig. 5.8.e resembles the spectral behaviour of the reference curve but with an abrupt spectral transition in band 450. This clearly shows the potential of a bilateral filtering scheme for the preservation of the spectral resolution when compensating for SN.

5.4 Summary

In this chapter we have evaluated the effectiveness of the noise compensation algorithms proposed in Section 4. Further, we have tested the performance of the algorithms when the hyperspectral data is affected by different types of stripe pat-

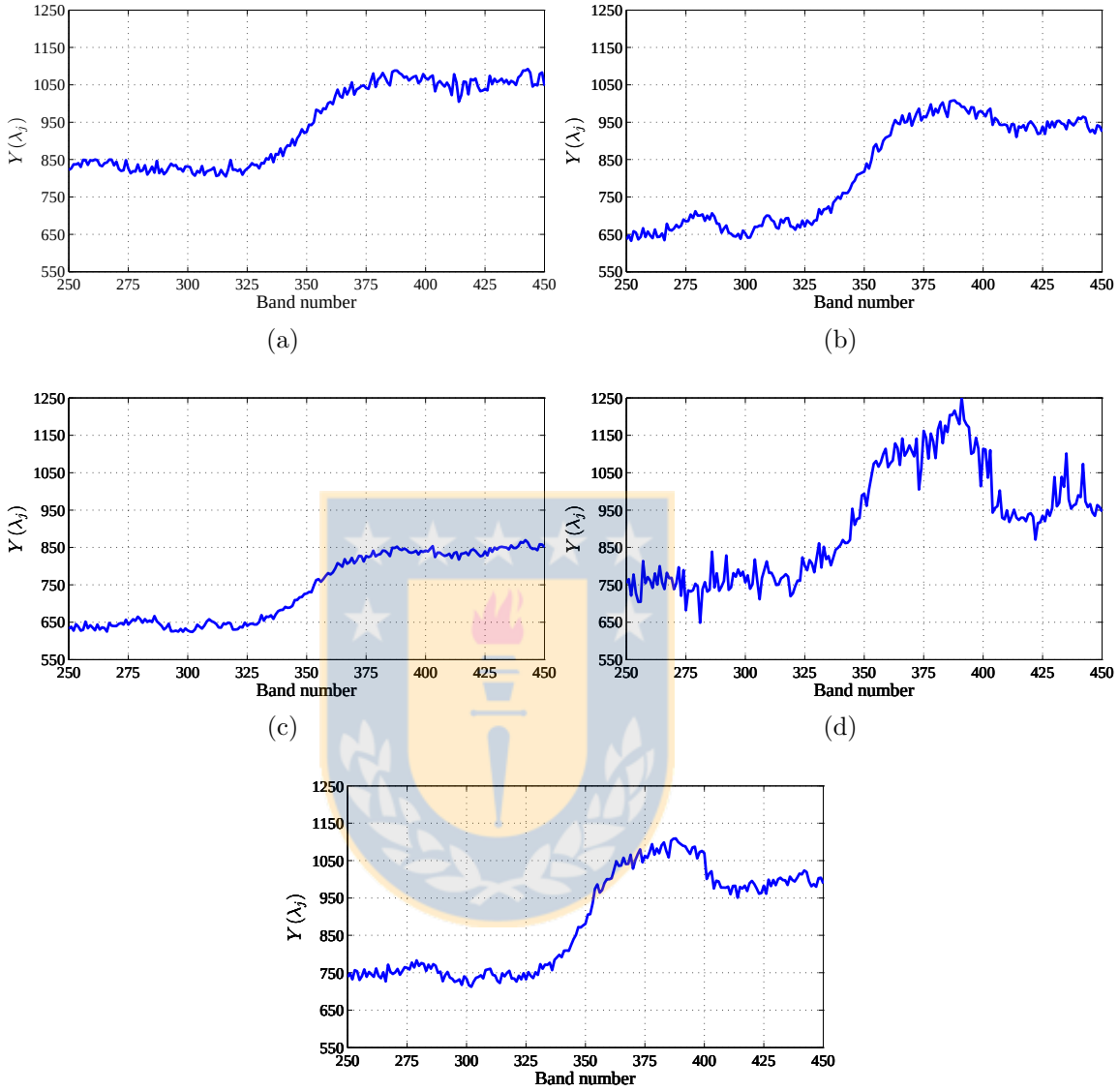

Figure 5.7: Hypercube 1: Spectral curves for the fixed spatial point 400 at the frame 800 and considering information from 151 neighboring spectral bands. (a) Reference. SN compensated spectral curves obtained using Model 1 and the (b) NN algorithm. SN compensated spectral curves obtained using Model 2 and the: (c) NN algorithm; (d) NN algorithm with the BF modification and $\sigma_r = 5$; and (e) NN algorithm with the BF modification and $\sigma_r = 25$.

terns.

We have successfully exploited the spectral redundancy concept and proposed two

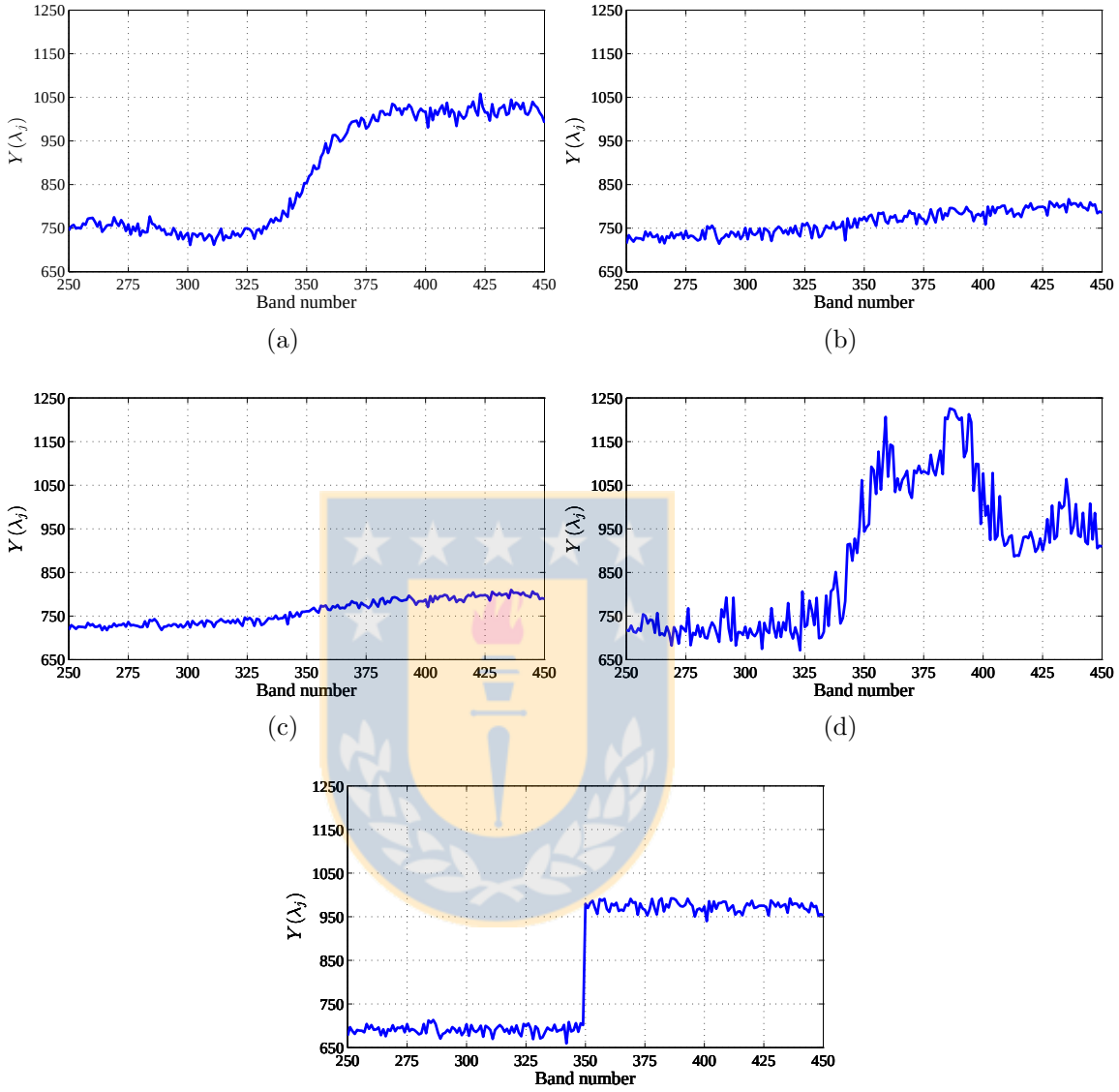

Figure 5.8: Hypercube 2: Spectral curves for the fixed spatial point 300 at the frame 800 and considering information from 151 neighboring spectral bands. (a) Reference. SN compensated spectral curves obtained using Model 1 and the (b) NN algorithm. SN compensated spectral curves obtained using Model 2 and the: (c) NN algorithm; (d) NN algorithm with the BF modification and $\sigma_r = 5$; and (e) NN algorithm with the BF modification and $\sigma_r = 25$.

efficient multidimensional algorithms for SNC in hyperspectral imaging systems. Furthermore, the SN has been addressed from an optoelectronic point of view, integrating

prior knowledge into the compensation schemes. The results observed in Section 5.2 indicates a good performance of the SNC algorithms when they are extended over the spectral domain. The multidimensional NN and the MM algorithms reduce the artifacts produced during the parameter estimation of noise, as shown in Figs. 5.1 and 5.2. Furthermore, it should be noted that both algorithms were designed to maintain the spatial fidelity of the assembled spectral image by fixing a low value of ΔI, equal to 0 in the case of the MM scheme. Nevertheless, depending on the spatial structure of the captured scene, an even better compensated image could be generated by increasing this value.

In Section 5.3 it is experimentally verified how the proposed compensation schemes are negatively affected when the FPA suffers from a stripe-like noise pattern (highly correlated noise between bands). That is, by having the same noise pattern on each band and due to the spectral redundancy assumption, the subset of spectral images does not contribute with additional information during the compensation process. It should be remarked that the readout electronics is the dominant source of structured noise. In this sense, if the design of the electronics determines the type of noise pattern observed in the hypercube, its should be used as prior knowledge in the noise compensation scheme.

In Section 5.4, the spectral signature is modified when the spectral redundancy assumption is not fulfilled. Also, by comparing the noise compensation capabilities together with the level of spectral modification of each algorithm, we are able to determine the best scheme to follow. The effectiveness of the BF modification is clear when observing the reassembled images in Fig. 5.6 and the spectral signatures in Fig. 5.8. That is, to achieve an effective noise compensation in the selected spectral image, while keeping the shape of the measured spectral signature. The compensation level observed when using the BF can be increased by following an estimation scheme to determine the optimal σ_r parameter. Such as, selecting a σ_r value equal to the overall standard deviation of the noise present in the raw data.

Chapter 6

Conclusion and Future Work

In this chapter, conclusions derived from this work are presented and detailed. Also, the tentative future research due to the results of the thesis are outlined below.

6.1 Conclusions

In this thesis, the spectral redundancy concept has been successfully exploited and two novel multidimensional algorithms for SNC in hyperspectral imaging systems are proposed. Furthermore, the SN has been addressed from an optoelectronic point of view, instead of just using digital image processing techniques, obtaining remarkable results. Namely, the algorithms use a novel pixel wise, affine image-degradation model, which assumes that the SN parameters are spatially uncorrelated, spectrally independent, and decoupled from camera's spectral response.

The experimental characterization performed in this work is a fundamental task for supporting the statements made during the design of the SNC process. In particular, results regarding the spectral dependence verify the relationship between SN parameters and the type of readout architecture used by the cameras, having a profound impact on the design of the SNC algorithms. Further, the low temporal drift of the SN parameters ensures that the noise pattern remains constant during the acquisition of a target scene. Also, the low spectral crosstalk observed in both hyperspectral cameras allows to disregard such effect in the model.

The research conducted here has shown that the use of a large number of bands, supported by the spectral redundancy concept, increases the performance of unidi-

mensional SNC algorithms. This idea has been tested on hyperspectral data exhibiting different stripe patterns on each band. The experiments have demonstrated that the proposed methods not only compensate for the SN, but also are able to render filtered images with fewer ghosting artifacts, which are normally induced during the parameter estimation. The results obtained by the BF modification applied over the NN algorithm are certainly encouraging. The modification provides means for weighting the spectral information in neighboring bands as function of their similarity with respect to the central band. The latter allows us to relax the assumption on the spectral redundancy, extending the applicability of multidimensional SNC algorithms to scenes with greater spectral variability.

Furthermore, it has been proven that highly correlated stripe patterns between neighboring spectral bands diminish the amount of useful spectral information for SNC. In this regard, our results using the NIR hyperspectral camera and the satellite imagery from the CHRIS/PROBA sensor have shown that the estimated parameters obtained with the multidimensional approach proposed here perform similarly to an unidimensional approach due to the lack of additional spectral information.

Finally, it should be remarked that the performance metric ρ_{SN} has proven to be useful for measuring levels of SN in corrupted images. That is, focusing only on spatial structures that produce high frequency components in the same direction as the SN and scoring results in accordance with the performance metrics traditionally used.

6.2 Contribution to Knowledge

- A novel pixel wise, affine image-degradation model for PBHCs is proposed by considering an optoelectronic approach, and thereby generating an accurate mathematical representation of the hyperspectral acquisition process.

- Decoupling the system spectral response from the multiplicative SN term have proven to be beneficial when designing a SNC algorithm for hyperspectral push-broom scanners.

- To our knowledge, the noise structure for PBHCs have been never explained from the point of view of the readout structure. In this sense, the model include

the capability for abstracting practical readout architectures such as APS and PPS, which are known to generate different noise patterns.

- Two novel multidimensional SNC algorithms for PBHCs have been developed, the multidimensional NN and MM algorithms. Both algorithms successfully exploit the spectral redundancy assumption, achieving remarkable results for the spectral compensated images when compared to the unidimensional case.

- In order relax the spectral redundancy assumption, a BF algorithm is proposed. The preliminary results obtained in this thesis exhibit the potential for maintaining the spectral detail when using a multidimensional scheme.

- The experimental data used in this thesis is available to the scientific community at the following address `https://www.dropbox.com/sh/qudw8camw2fz03m/YBuN_nvfZ5`.

6.3 Future Work

Recapitulating the results obtained from this work, we extract that the adaptability of the proposed SNC algorithms must be verified using different hyperspectral technologies, spectral bands, and spectral resolutions. Also, the SNC performed by the NN algorithm could be improved by selecting a different learning rate for each spectral image according to the variability of the acquired spatio-spectral information.

During the design of the SNC algorithms, we have assumed that the SN parameters are not correlated between spectral bands. However, when the parameters are highly correlated, it is possible to take advantage of this information by modifying the SNC procedure. Namely, designing an algorithm that uses the information from the SN parameters spectral structure, without discriminating on the type of spectral correlation exhibited in the hypercube.

Appendix A

Summary of Contributions

As a result of work done in the course of this thesis, there have been various publications oriented to fulfilling the objectives initially proposed.

- Chapter 2 was partially presented at the SPIE Infrared Sensors, Devices, and Applications; and Single Photon Imaging II held in San Diego, CA, USA, in 2011 [A.2.2]. A preliminary version of the observation model was accepted for publication at *Elsevier Infrared Physics & Technology* in 2014 [A.1.3].

- Chapter 3 was partially presented at the SPIE Electro-Optical Remote Sensing, Photonic Technologies, and Applications VI Conference held in Edinburgh, UK in 2012 [A.2.1]. The results of the hyperspectral calibration where used in the article accepted for publication at *AMB Express* in 2013 [A.1.2].

- Chapter 4 was preliminarily developed in the article published at Optic Letters in 2010 [A.1.4], and then further developed in the an article submitted to *Transactions on Geosciences and Remote Sensing* in 2013 [A.1.1], still in peer-review.

- Chapter 5 was submitted to *Transactions on Geosciences and Remote Sensing* in 2013 [A.1.1], still in peer-review.

A.1 Journal Papers

A.1.1 P. Meza, J. E. Pezoa, and S. N. Torres, "Multidimensional Striping Noise Compensation in Hyperspectral Imaging: Exploiting Hypercubes' Spatial, Spectral, and Temporal Redundancy," submitted to *Transactions on Geosciences and Remote Sensing*, November 2013.

A.1.2 M. J. Gallardo, J. P. Staforelli, P. Meza, I. Bordeu, and S. N. Torres, "Characterization of Chromobacterium violaceum pigment through a Hyperspectral Imaging System," accepted in *AMB Express*, December 2013.

A.1.3 F. Parra, P. Meza, S. N. Torres, J. E. Pezoa, and H. Mella, "Modeling and Compensating Non-Uniformity in Push-broom NIR Hyperspectral Imaging System", accepted in *Elsevier Infrared Physics & Technology*, January 2014.

A.1.4 E. Vera, P. Meza, and S. N. Torres, "Total variation approach for adaptive nonuniformity correction in focal-plane arrays," *Opt. Lett.*, **36**(2), pp. 172-174, 2011.

A.2 Conference Papers

A.2.1 P. Meza, J. E. Pezoa, F. Parra, and S. N. Torres (2012) "A prior knowledge model for multidimensional striping noise compensation in hyperspectral imaging devices," in *Electro-Optical Remote Sensing, Photonic Technologies, and Applications VI*, vol. 8542, SPIE, p. 854222.

A.2.2 P. Meza, F. Parra, S. N. Torres, J. E. Pezoa, and P. Coelho (2011) "A multidimensional approach for striping noise compensation in hyperspectral imaging devices," in *Infrared Sensors, Devices, and Applications; and Single Photon Imaging II*, vol. 8155, SPIE, p. 81550I.

A.3 Additional Publications

It also detailed other publications that i was involved as author and/or co-author during the course of the doctoral program.

A.3.1 F. Parra, J. E. Pezoa, P. Meza, S. N. Torres, and O. Zapata (2012) "On the thermal-offset in NIR hyperspectral cameras," in *Thermosense: Thermal Infrared Applications XXXIV*, vol. 8354, SPIE, p. 835411.

A.3.2 C. San Martin, C. Deocares, S. Godoy, P. Meza, and D. Bonilla (2012) "Wavelet-FFT Filter Applied to Non Uniformity Correction in Infrared Imaging System," in *Progress in Pattern Recognition, Image Analysis, Computer Vision, and Applications*, vol. 7441, LNCS, p. 355-363.

A.3.3 F. Parra, P. Meza, J. E. Pezoa, and S. N. Torres (2011) "Thermal characterization of a NIR hyperspectral camera," in *Electro-Optical Remote Sensing, Photonic Technologies, and Applications V*, vol. 8186, SPIE, p. 81860Z.

A.3.4 F. Parra, P. Meza, C. Toro, and S. N. Torres (2011) "Infrared Focal Plane Array Imaging System Characterization by Means of a Blackbody Radiator," in *Progress in Pattern Recognition, Image Analysis, Computer Vision, and Applications*, vol. 7042, LNCS, p. 105-112.

A.3.5 E. Vera, P. Meza, and S. N. Torres (2010) "Total Variation Adaptive Scene-Based Nonuniformity Correction," in *Imaging Systems*, OSA, p. JTuA24.

A.3.6 P. Meza, C. San Martin, E. Vera, and S. N. Torres (2010) "A Quantitative Evaluation of Fixed-Pattern Noise Reduction Methods in Imaging Systems," in *Progress in Pattern Recognition, Image Analysis, Computer Vision, and Applications*, vol. 6419, LNCS, p. 285-294.

A.3.7 P. Meza, E. Vera, S. Godoy, and S. N. Torres (2010) "A New Reference-free Infrared Image Quality Metric for Nonuniformity Correction," in *Proceedings of the 14th World Multi-Conference on Systemics, Cybernetics and Informatics: WMSCI*.

Appendix B

Experimental Equipment

B.1 Datasheet

The following document are included in the Appendix:

i Spectral Camera Test Report: Photonfocus Hurricane-40

ii Spectral Camera Test Report: Xenics XEVA-USB 2.0

iii Calibrated Light Source: QTH Calibration Source M-63978

iv Calibrated Light Source: AR-1 Argon Calibration Source

v Calibrated Light Source: AR-1 Argon Calibration Source

vi Diffuse Reflectance Target: Spectralon SRT-99-120

Spectral Camera Test Report

Spectral Camera

Spectral camera model	PFH
Camera model	Photonfocus Hurricane-40
Sensor type	10.85x10.85mm -1024x1024 pixels
Camera serial number	013500004047
Spectrograph model	V10E 2/3"
Spectrograph serial number	V10E_1107_221
Grating serial number	V170_0307_2x
Slit size / µm	30
Nominal spectral range / nm	400 - 1000
Nominal spectral resolution / nm	2.73
Nominal spatial bending / nm	0.125
Numerical aperture	2.4

Measurement setup

Camera model	Photonfocus Hurricane-40
Sensor type	10.85x10.85mm -1024x1024 pixels
Calibration sources	- HgAr calibration lamp - Calibrated radiance standard
Filters	OG-590

Test results

Spectral resolution

Spectral resolution according to the Rayleigh criterion

Peak / nm	FWHM / nm
435.8	2.9
696.5	2.91
912.3	2.94

Optical characteristics

Straylight at 545 nm - 547 nm	1.2%
Spectral range / nm	245 - 1331
Spatial bending (smile) acceptable	Yes
Visible ghost lines or images	No
Wavelength calibration equation	y = 8.193e-005*x^2 + 0.97514*x + 240.695

Mechanical characteristics

Appearance checked	Yes
Camera mount checked	Yes
Fore lens mount checked	Yes

Diffraction efficiency

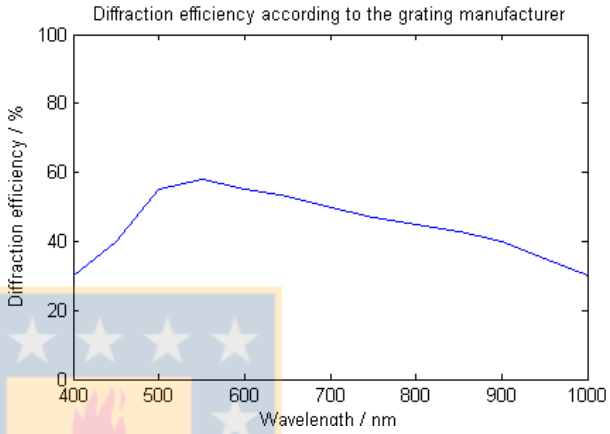

Spectrum lamp images

Captured image - HgAr calibration lamp

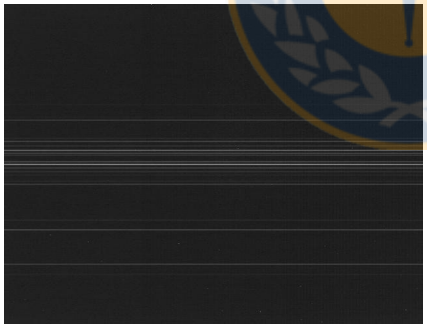

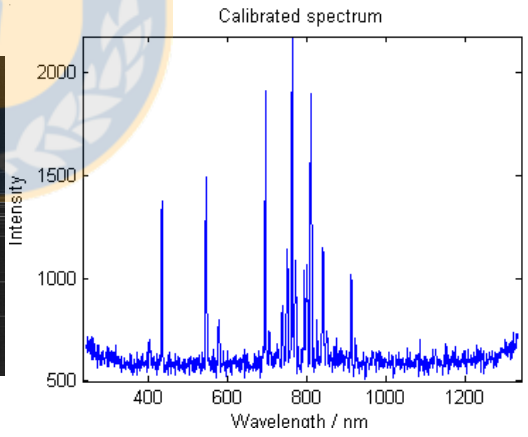

Notes

Tested and approved by

191107 / MAU

Spectral Camera Test Report

Spectral Camera	Spectral camera model	NIR (USB)
	Camera model	Xenics XEVA-USB 2.0
	Sensor type	8.8x6.6mm -320x256 pixels
	Camera serial number	XEVA-545
	Spectrograph model	N17E 2/3"
	Spectrograph serial number	N17E_1207_97
	Grating serial number	V156_1006_18
	Slit size / µm	30
	Nominal spectral range / nm	900 - 1700
	Nominal spectral resolution / nm	3.64
	Nominal spatial bending / nm	0.35
	Numerical aperture	2

Measurement setup	Camera model	Xenics XEVA-USB 2.0
	Sensor type	8.8x6.6mm -320x256 pixels
	Calibration sources	
	Filters	LPF-1400

Test results

Spectral resolution

Spectral resolution according to the Rayleigh criterion

Peak / nm	FWHM / nm
1129	4.6
1357	4.0
1530	4.7

Optical characteristics	Straylight at 1300 nm - 1324 nm	1.5%
	Spectral range / nm	880 - 1750
	Spatial bending (smile) acceptable	Yes
	Visible ghost lines or images	No
	Wavelength calibration equation	y = 0.00060434*x^2 + 3.258*x + 876.719
Mechanical characteristics	Appearance checked	Yes
	Camera mount checked	Yes
	Fore lens mount checked	Yes

Diffraction efficiency

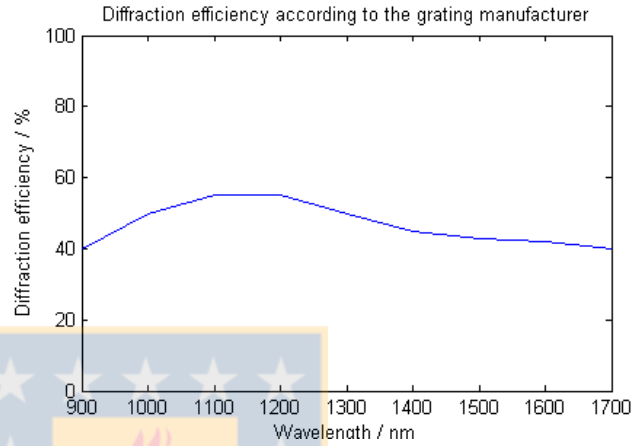

Spectrum lamp images

Captured image

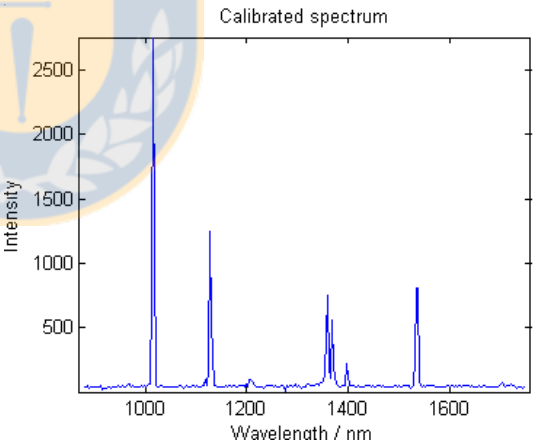

Notes

Tested and approved by

10.12.2007 HKA

Oriel Calibrated Sources and Services

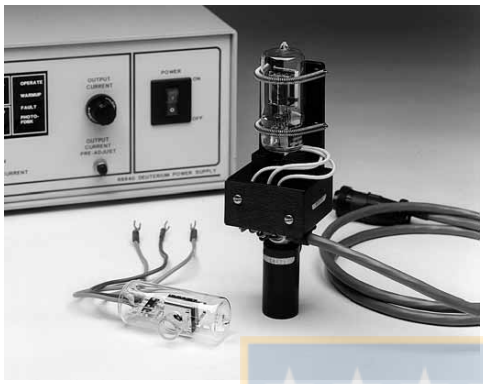

63945 Calibrated Deuterium Lamp

These NIST traceable calibrated lamps are reliable sources of known spectral irradiance in the UV and VIS-NIR. Use these systems to calibrate your own irradiance source, or to transfer our NIST traceable calibration to a spectroscopic detection system. We offer deuterium and quartz tungsten halogen irradiance standards as individual lamps and as complete sources, which include a Radiometric Power Supply, lamp mount and lamp (with calibration data).

NIST Traceable

Each of our calibrated lamps is thoroughly tested to specification. Lamps are preconditioned and selected as necessary. The irradiance measurements are taken in our specially outfitted calibration laboratory. In the U.S., the National Institute of Standards and Technology (NIST) provides original uncertainties for their standard lamps. This range varies according to wavelength and lamp structure. There is an additional, small, uncertainty introduced during our procedure. Tables 1 and 2 show both (NIST and Newport's) uncertainty values for the 1000 W QTH and 30 W deuterium lamps.

Table 1 k = 2 Uncertainty Values for 63978 1000 W QTH Source

Wavelength (nm)	Approximate NIST Uncertainty (%)	Approximate Newport's Uncertainty* (%)
250	2.23	2.8
350	1.35	2.5
654.6	1.01	2.5
900	1.34	2.5
1300	1.42	2.5
1600	1.89	2.8
2000	3.29	2.8
2400	6.50	2.8

* Additional uncertainty due to calibration transfer.
Note: the uncertainty values can vary from time to time.

Table 2 k = 2 Uncertainty Values for 63979 30 W Deuterium Source

Wavelength Range (nm)	Approximate NIST Uncertainty (%)	Approximate Newport's Uncertainty* (%)
200	1.1	3.0
210	1.0	3.0
250	1.0	3.0
350	1.0	3.0

* Additional uncertainty due to calibration transfer.
Note: the uncertainty values can vary from time to time.

Produce Your Own Standard

Lamps have a limited life. If you use the lamp frequently, we recommend that you purchase one or more non-calibrated lamps to produce your own working standard(s).

Which Source Do I Choose?

We offer three types of calibrated irradiance sources:

Calibrated QTH Sources

- 250 - 2400 nm or 300 - 2400 nm (lamp dependent) calibration range
- Offered in 45 W, 200 W and 1000 W powers

Calibrated Deuterium Sources

- 250 - 400 nm calibration range
- 30 W model, only

Custom Sources/Calibrations

- Calibrations of your lamp
- Custom standards

Choose a lamp that provides irradiance levels close to what you would like to measure in your wavelength range of interest. Using a lamp that produces too much or too little irradiance puts higher demands on the linearity of your detection system. If you need an irradiance standard below ~330 nm, choose the deuterium lamp. This lamp provides more UV radiation than the QTH lamps (see Fig. 1), is calibrated down to 200 nm, and has the additional advantage of producing very little visible light. The low level of visible and near IR radiation reduces the out of band problems that plague UV calibration of instruments based on silicon photodiodes and other broadband detectors.

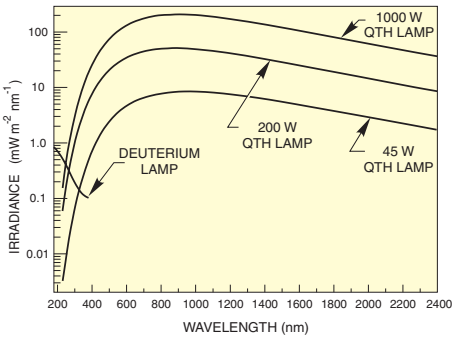

Fig. 1 Spectral irradiance of calibrated lamps

Open Air Lamp Mounts

Our Calibrated Lamps are run in open-air. The mounts holding the lamps are simple, rod-mounted holders. They have a 1/4-20 tapped hole in the base for an optical rod. The appropriate lamp mount for your lamp is included with each source - or you can purchase individually.

Calibration Services

Please contact a Newport Sales Engineer for a quote on your custom calibration requirement. Typically, an annual calibration is recommended for calibrated lamps - although calibration dramatically varies with lamp usage.

Safety Considerations

When there is no clear selection of lamp, based upon irradiance level, the working environment may make the determination. The proper way to operate these lamps for calibration is in our open-air mounts. Therefore, the lower power calibrated QTH lamps are significantly easier to work with. These lamps are as safe as any bright domestic bulb except for the emission of ultraviolet. The 1 kW lamp is uncomfortably bright and heats any absorbing surface close to it; no flammable material should be placed near the lamp. Conversely, the deuterium lamp produces little visible light but very intense UV radiation. In all cases, UV goggles should be worn and exposure to the skin should be minimized. Always post appropriate safety signs - (see page 246 for UV safety eyewear, gloves and UV safety signs).

Ordering Information

Complete Calibration Sources

All sources include lamp mount, power supply, your choice of calibrated lamp and all necessary cables.

Source Type	Wattage	Calibration Range (nm)	Model
QTH	45 or 200* W	300 - 2400 (for 45 W lamp) 250 - 2400 (for 200 W lamp)	63976
	1000 W	250 - 2400	63978
Deuterium	30 W	200 - 400	63979

* Choose between 45 and 200 W lamps when ordering this source; please note that the 45 W lamp is calibrated from 300 - 2400 nm. If you require calibration down to 250 nm, choose the 200 W lamps.

Calibrated Lamps

Lamp Type	Wattage	Calibration Range (nm)	Model
QTH	45 W	300 - 2400	63358
	200 W	250 - 2400	63355
	1000 W	250 - 2400	63350
Deuterium	30 W	200 - 400	63945

Non-Calibrated Lamps

Lamp Type	Wattage	Model
QTH	45 W	63360
	200 W	63368
	1000 W	63362
Deuterium	30 W	63946

For This Lamp Type	Lamp Model Numbers	Lamp Mount
45 or 200 W QTH	63358, 63355, 63360, 63368	63966
1000 W QTH	63350, 63362	63965

Note: Please check our product web pages for more technical information at www.newport.com.

HG-1 Mercury Argon Calibration Source

The **HG-1 Mercury Argon Calibration Source** is a wavelength calibration source for UV-VIS-Shortwave NIR spectrophotometric systems. The HG-1 produces Mercury and Argon lines from 253-922 nm, for use in performing fast, accurate spectrometer wavelength calibrations. The HG-1 has an SMA 905 termination for connecting to optical fibers.

Caution!

- The beam emerging from the HG-1 produces ultraviolet radiation. Direct contact with the beam could cause serious eye injury. Never look directly into the light source.
- *Never* take apart the HG-1. The HG-1 contains mercury. Dangerous voltages present. No user-serviceable parts inside.
- The SMA connector may get **HOT** during operation.

Setting Up

To re-calibrate the wavelength of your spectrometer, you will need the following:

- The HG-1 Mercury-Argon lamp
- Your spectrometer
- An optical fiber (for spectrometers without a built-in slit, a 50-µm fiber works best)
- Either a spreadsheet program (Excel or Quattro Pro, for example) or a calculator that performs third-order linear regressions. If you are using Microsoft Excel, choose **Tools | Add-Ins** and check **AnalysisToolPak** and **AnalysisToolPak-VBA**

Operation

1. Plug the wall transformer end of the HG-1's power supply into a standard 110 V outlet. Plug the 12 V output end into the back of your HG-1. Or, insert a 9V battery (not included).
2. Attach a fiber from the spectrometer into the SMA connector on your HG-1. If your spectrometer does not have an entrance slit, use a 50-µm diameter (or smaller) optical fiber. Larger fibers and slits will have lesser optical resolution. Also, keep in mind that if the spectrometer has no slit and your experimentation involves using optical fibers of different diameters, wavelength calibration with each fiber you anticipate using will be necessary. Calibration is also recommended each time you unscrew the fiber from the spectrometer.
3. Find the on/off switch next to the SMA connector and turn the lamp on. The red indicator will light when the lamp is on.

Calibration

You are going to be solving the following equation, which shows that the relationship between pixel number and wavelength is a third-order polynomial:

$$\lambda_p = I + C_1 p + C_2 p^2 + C_2 p^3$$

where λ is the wavelength of pixel p, I is the wavelength of pixel 0, C_1 is the first coefficient (nm/pixel), C_2 is the second coefficient (nm/pixel^2), and C_3 is the third coefficient (nm/pixel^3). You will be calculating the value for I and the three Cs.

6. The numbers of importance are indicated in the above figure. You will need to record the Intercept as well as the First, Second, and Third Coefficients. Also, look at the value for R squared. It should be *very* close to 1. If it is not, you have probably assigned one of your wavelengths incorrectly.
7. Select **Spectrometer | Configure** from the menu and choose the **Wavelength Calibration** page to update the wavelength coefficients within OOIBase32.
8. Repeat this process for each channel in your setup.

Spectral Output

Mercury emission lines are <600 nm. Argon emission lines are >600 nm, and are shown here on the right on an exaggerated amplitude scale. Below is a list of the most prominent mercury and argon peaks.

Mercury Lines	Argon Lines
253.65	696.54
296.73	706.72
302.15	710.75
313.16	727.29
334.15	738.40
365.01	750.39
404.66	763.51
407.78	772.40
435.84	794.82
546.08	800.62
576.96	811.53
579.07	826.45
	842.46
	852.14
	866.79
	912.30
	922.45

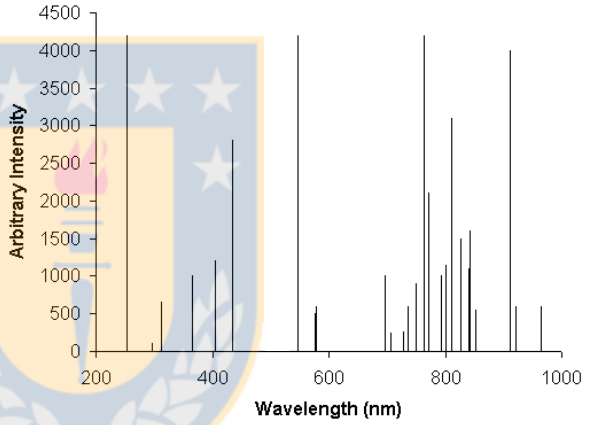

Specifications

Output:	low-pressure gas discharge lines of Mercury and Argon
Spectral range:	253-922 nm
Dimensions:	11.4 cm x 6.98 cm x 2.54 cm (LWH), 4.5" x 6.98" x 1.0" (LWH)
Power requirements:	12 VDC wall transformer (comes with unit) **or** 9 VDC battery
Internal voltage:	600 volts at 30 kHz
Bulb life:	~3,500 hours
Amplitude stabilization:	~1 minute
Aperture:	3 mm
Connector:	SMA 905

AR-1 Argon Calibration Light Source

The AR-1 Argon Calibration Source is a wavelength calibration source for Ocean Optics NIR-256 and NIR-512 Spectrometers. The AR-1 produces Argon lines from 866-1705 nm, and is an ideal lamp to use when performing fast, accurate spectrometer wavelength calibrations in the NIR range.

The AR-1 features an SMA 905 Connector for interfacing with our optical fibers. It operates with a 12 VDC power supply (included with the unit) or 9V battery (not included).

The following sections detail the features of the AR-1 Argon Calibration Light Sources.

Note: The AR-1 is NOT designed to operate as an excitation source in your experiments.

Parts Included

The AR-1 ships with the following items:

- AR-1 Argon Calibration Light Source
- 12 VDC power supply

Warnings

- The SMA 905 Connector may get extremely hot during lamp operation. After use, allow sufficient time to cool before handling.
- Dangerous voltages are present, and there are no user-serviceable parts inside. Do not open the AR-1.

Using the AR-1

The following sections provide instructions on setting up the AR-1 light source and performing a wavelength calibration using the AR-1:

Configuring the AR-1

Follow the steps below to configure the AR-1:

1. Plug the 12 VDC power supply into a power outlet, then connect the barrel connector of the power supply to the power input on the rear of the AR-1.

   Alternately, you can use a 9-volt battery (not included) to power the AR-1. Open the battery hatch of the AR-1 and install the 9-volt battery, then proceed to Step 2.

2. Connect a fiber to the SMA 905 Connector on the AR-1. If your spectrometer does not have an entrance slit, use a 50 µm diameter (or smaller) fiber. Larger fibers and slits result in reduced optical resolution.

   Please note that if the spectrometer does not have a slit and your experiment requires you to use fibers of varying diameters, you will need to perform a wavelength calibration. You should also perform a wavelength calibration each time you unscrew the fiber from the spectrometer.

3. Move the On/Off switch on the AR-1 (next to the SMA 905 Connector) to the On position. The red LED will illuminate to indicate that the AR-1 is powered on.

You have now configured the AR-1 for use. Proceed to the next section for wavelength calibration instructions.

AR-1 Argon Calibration Light Source

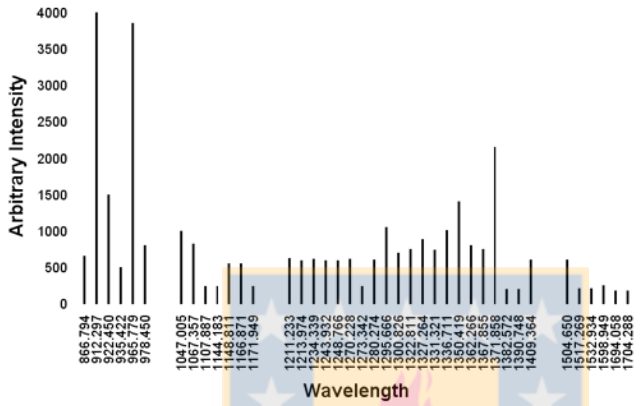

AR-1 Specifications

Output	Low-pressure gas discharge lines of Argon
Dimensions (in mm):	125.7 x 70 x 25.8
Power consumption:	250 mA at 12 VDC
Power requirements:	12 VDC wall transformer (included) or 9 VDC battery (optional)
Bulb life:	Approx. 3500 hours (at 20 mA)
Internal voltage:	600 volts at 30 kHz
Aperture:	3 mm
Amplitude stabilization:	~ 1 minute
Connector:	SMA 905

DIFFUSE REFLECTANCE TARGETS

Durable Reflectance Panels for Laboratory and Field Applications under Harsh Conditions

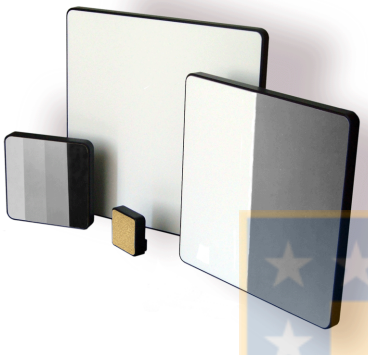

FEATURES

Durable and Washable
Various Reflectances Available
Impervious to Harsh Environments

APPLICATIONS

Backlight Illuminators
Environmental Test Targets
Laser Targets
Optical Reflectors
Remote Sensing Targets

SPECTRALON® TARGETS

Spectralon targets are ideal for laboratory and field applications that require long exposure to harsh environmental conditions. Because of the diffuse reflectance properties of Spectralon, these targets maintain a constant contrast over a wide range of lighting conditions.

Spectralon targets are available in plates up to 24" x 24" in white or gray material, mounted in a rugged anodized aluminum frame. Calibration data from 250 to 2500 nm, every 50 nm is supplied with the targets and is traceable to the National Institute of Standards and Technology (NIST). All targets are thermally and chemically stable and easily cleaned. Custom targets of various reflectance values are also available up to 3 m x 3 m.

SPECTRALON® CONTRAST TARGETS

Spectralon Contrast Targets are perfect for the calibration of video cameras, densitometers, the contrast transfer of propagation media, and the testing of imaging systems in field conditions.

These chemically inert targets are durable and washable, consisting of a diffuse white (99% reflectance) and a diffuse gray (10% reflectance) panel mounted side-by-side in an anodized aluminum frame.

Spectralon multi-step targets consist of four panels of 99, 50, 25 and 12% reflectance mounted side-by-side. The four panels provide equal optical density differences and equal contrast between each adjacent panel.

TYPICAL 8° HEMISPHERICAL REFLECTANCE SRM-990

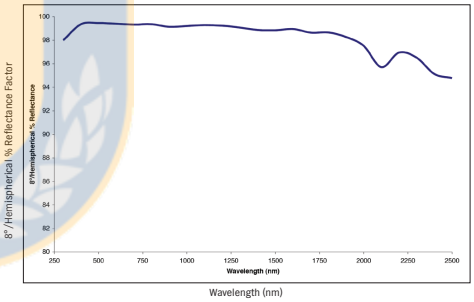

Wavelength (nm)

TABLE 1: Corrected Reflectance Values for 99% Spectralon Targets

Wavelength Range (nm)	8°/Hemispherical Spectral Reflectance Values
250	0.925[1]
300	0.925
350	0.975 - 0.995
500 - 700	0.985 - 0.995
750 - 1600	0.975 - 0.995
1650 - 2500	0.925

[1] If the 99% material is not contained in a Delrin or Aluminum cup, the minimum reflectance is 0.900 at 250 nm.

TABLE 2: Acceptable 8°/Hemispherical Corrected Reflectance Factors for Gray Spectralon Targets

Nominal Reflectance	Tolerance at 600 nm	Flatness Range over 350 - 760 nm
2 - 5%	± 2%	± 4%
6 - 19%	± 3%	± 5%
20 - 95%	± 5%	± 5%

Labsphere, Inc. · 231 Shaker St. · North Sutton, NH 03260 · USA · Tel: +1 603 927 4266 · www.labsphere.com
PB-13025-000 Rev 00

SPECIFICATIONS

Spectralon® Diffuse Reflectance Targets. Refer to Tables 1 & 2 for Tolerances.

Target part no.	Reflectance Value	Reflective Area (inches)	Size Mounted (LxWxH inches)	Order Number
SRT-02-020	2%	2 x 2	2.25 x 2.25 x 0.56	AA-00823-900
SRT-02-050	2%	5 x 5	5.25 x 5.25 x 0.56	AA-00821-900
SRT-02-100	2%	10 x 10	10.25 x 10.25 x 0.56	AA-00822-900
SRT-02-120	2%	12 x 12	12.25 x 12.25 x 0.56	AA-00827-900
SRT-02-180	2%	18 x 18	18.25 x 18.25 x 0.56	AA-00826-900
SRT-02-240	2%	24 x 24	24.25 x 24.25 x 0.56	AA-00837-900
SRT-05-020	5%	2 x 2	2.25 x 2.25 x 0.56	AA-00823-800
SRT-05-050	5%	5 x 5	5.25 x 5.25 x 0.56	AA-00821-800
SRT-05-100	5%	10 x 10	10.25 x 10.25 x 0.56	AA-00822-800
SRT-10-020	10%	2 x 2	2.25 x 2.25 x 0.56	AA-00823-700
SRT-10-050	10%	5 x 5	5.25 x 5.25 x 0.56	AA-00821-700
SRT-10-100	10%	10 x 10	10.25 x 10.25 x 0.56	AA-00822-700
SRT-20-020	20%	2 x 2	2.25 x 2.25 x 0.56	AA-00823-600
SRT-20-050	20%	5 x 5	5.25 x 5.25 x 0.56	AA-00821-600
SRT-20-100	20%	10 x 10	10.25 x 10.25 x 0.56	AA-00822-600
SRT-40-020	40%	2 x 2	2.25 x 2.25 x 0.56	AA-00823-500
SRT-40-050	40%	5 x 5	5.25 x 5.25 x 0.56	AA-00821-500
SRT-40-100	40%	10 x 10	10.25 x 10.25 x 0.56	AA-00822-500
SRT-50-020	50%	2 x 2	2.25 x 2.25 x 0.56	AA-00823-400
SRT-50-050	50%	5 x 5	5.25 x 5.25 x 0.56	AA-00821-400
SRT-50-100	50%	10 x 10	10.25 x 10.25 x 0.56	AA-00822-400
SRT-50-120	50%	12 x 12	12.25 x 12.25 x 0.56	AA-00827-400
SRT-50-180	50%	18 x 18	18.25 x 18.25 x 0.56	AA-00826-400
SRT-50-240	50%	24 x 24	24.25 x 24.25 x 0.56	AA-00837-400
SRT-60-020	60%	2 x 2	2.25 x 2.25 x 0.56	AA-00823-300
SRT-60-050	60%	5 x 5	5.25 x 5.25 x 0.56	AA-00821-300
SRT-60-100	60%	10 x 10	10.25 x 10.25 x 0.56	AA-00822-300
SRT-75-020	75%	2 x 2	2.25 x 2.25 x 0.56	AA-00823-200
SRT-75-050	75%	5 x 5	5.25 x 5.25 x 0.56	AA-00821-200
SRT-75-100	75%	10 x 10	10.25 x 10.25 x 0.56	AA-00822-200
SRT-75-120	75%	12 x 12	12.25 x 12.25 x 0.56	AA-00827-200
SRT-75-180	75%	18 x 18	18.25 x 18.25 x 0.56	AA-00826-200
SRT-75-240	75%	24 x 24	24.25 x 24.25 x 0.56	AA-00837-200
SRT-80-020	80%	2 x 2	2.25 x 2.25 x 0.56	AA-00823-100
SRT-80-050	80%	5 x 5	5.25 x 5.25 x 0.56	AA-00821-100
SRT-80-100	80%	10 x 10	10.25 x 10.25 x 0.56	AA-00822-100
SRT-99-020	99%	2 x 2	2.25 x 2.25 x 0.56	AA-00823-000
SRT-99-050	99%	5 x 5	5.25 x 5.25 x 0.56	AA-00821-000
SRT-99-100	99%	10 x 10	10.25 x 10.25 x 0.56	AA-00822-000
SRT-99-120	99%	12 x 12	12.25 x 12.25 x 0.56	AA-00827-000
SRT-99-180	99%	18 x 18	18.25 x 18.25 x 0.56	AA-00826-000
SRT-99-240	99%	24 x 24	24.25 x 24.25 x 0.56	AA-00837-000

Spectralon® Contrast Targets

Target Part No.	Type	Reflectance Values	Reflective area (inches)	Order Number
SRT-SP-050	Split	99, 10%	5 x 5	AA-00656-000
SRT-SP-100	Split	99, 10%	10 x 10	AA-00657-000
SRT-SP-180	Split	99, 10%	18 x 18	AA-00658-000
SRT-MS-050	Multi-step	99, 50, 25, 12%	5 x 5	AA-00659-000
SRT-MS-100	Multi-step	99, 50, 25, 12%	10 x 10	AA-00660-000
SRT-MS-180	Multi-step	99, 50, 25, 12%	18 x 18	AA-00661-000

Bibliography

[1] M. Borengasser, W. S. Hungate, and R. L. Watkins, *Hyperspectral Remote Sensing: Principles and Applications* (CRC Press, 2008).

[2] D.-W. Sun, *Hyperspectral Imaging for Food Quality Analysis and Control* (Academic Press, 2010), 1st ed.

[3] C. J. Hirschmugl and K. M. Gough, "Fourier transform infrared spectrochemical imaging: Review of design and applications with a focal plane array and multiple beam synchrotron radiation source," Appl. Spectrosc. **66**, 475–491 (2012).

[4] P. Ardouin, J. Levesque, and T. Rea, "A demonstration of hyperspectral image exploitation for military applications," in "Information Fusion, 2007 10th International Conference on," (2007), pp. 1–8.

[5] L. Gómez-Chova, L. Alonso, L. Guanter, G. Camps-Valls, J. Calpe, and J. Moreno, "Correction of systematic spatial noise in push-broom hyperspectral sensors: application to CHRIS/PROBA images," Appl. Opt. **47**, F46–F60 (2008).

[6] N. Acito, M. Diani, and G. Corsini, "Subspace-based striping noise reduction in hyperspectral images," Geoscience and Remote Sensing, IEEE Transactions on **49**, 1325–1342 (2011).

[7] B. E. A. Saleh and M. C. Teich, *Fundamentals of photonics* (Wiley-Interscience, New York [u.a.], 1991).

[8] A. E. Gamal, B. A. Fowler, H. Min, and X. Liu, "Modeling and estimation of fpn components in cmos image sensors," in "Solid State Sensor Arrays: Development and Applications II," , vol. 3301, M. M. Blouke, ed. (SPIE, 1998), vol. 3301, pp. 168–177.

[9] H. T. Boyd, H. Tian, B. Fowler, and A. E. Gamal, "Analysis of temporal noise in cmos photodiode active pixel sensor," IEEE Journal of Solid-State Circuits **36**, 92–101 (2001).

[10] R. Leathers, T. Downes, and R. Priest, "Scene-based nonuniformity corrections for optical and swir pushbroom sensors," Opt. Express **13**, 5136–5150 (2005).

[11] F. Gadallah and F. Csillag, "Destriping multisensor imagery with moment matching," International Journal of Remote Sensing **21**, 2505–2511 (2000).

[12] P. Rakwatin, W. Takeuchi, and Y. Yasuoka, "Stripe noise reduction in MODIS data by combining histogram matching with facet filter," IEEE Transactions on Geoscience and Remote Sensing **45**, 1844–1856 (2007).

[13] W.-W. Chang, L. Guo, Z.-Y. Fu, and K. Liu, "A new destriping method of imaging spectrometer images," in "Wavelet Analysis and Pattern Recognition, 2007. ICWAPR 2007. International Conference on," , vol. 1 (2007), vol. 1, pp. 437–441.

[14] J. Chen, Y. Shao, H. Guo, W. Wang, and B. Zhu, "Destriping CMODIS data by power filtering," IEEE Transactions on Geoscience and Remote Sensing **41**, 2119–2124 (2003).

[15] C. Chang-Yan, Z. Ji-Xian, and L. Zheng-Jun, "Study on methods of noise reduction in a stripped image," International Archives of the Photogrammetry, Remote Sensing and Spatial Information Sciences **37**, 213–216 (2008).

[16] J. Chen, H. Lin, Y. Shao, and L. Yang, "Oblique striping removal in remote sensing imagery based on wavelet transform," International Journal of Remote Sensing **27**, 1717–1723 (2006).

[17] B. Munch, P. Trtik, F. Marone, and M. Stampanoni, "Stripe and ring artifact removal with combined Wavelet–Fourier filtering," Opt. Express **17**, 8567–8591 (2009).

[18] H. Shen and L. Zhang, "A map-based algorithm for destriping and inpainting of remotely sensed images," Geoscience and Remote Sensing, IEEE Transactions on **47**, 1492–1502 (2009).

[19] L. Sun, R. Neville, K. Staenz, and H. P. White, "Automatic destriping of hyperion imagery based on spectral moment matching," Canadian Journal of Remote Sensing **34**, S68–S81 (2008).

[20] P. Meza, F. Parra, S. N. Torres, J. E. Pezoa, and P. Coelho, "A multidimensional approach for striping noise compensation in hyperspectral imaging devices," Proc. SPIE **8155**, 81550I (2011).

[21] S.-L. Chen, X.-Y. Hu, and S.-L. Peng, "Hyperspectral imagery denoising using a spatial-spectral domain mixing prior," Journal of Computer Science and Technology **27**, 851–861 (2012).

[22] C. Tomasi and R. Manduchi, "Bilateral filtering for gray and color images," in "Computer Vision, 1998. Sixth International Conference on," (1998), pp. 839–846.

[23] H. Peng, R. Rao, and D. W. Messinger, "Spatio-spectral bilateral filters for hyperspectral imaging," (2008), vol. 6966, pp. 69660O–69660O–7.

[24] K. Nummedal, "Wide-field imagers-pushbroom or whiskbroom scanners," (1980), vol. 0226, pp. 38–52.

[25] J. Hill, *Remote Sensing and Geographical Information Systems for Resource Management in Developing Countries* (Kluwer Academic Publishers, 1991), vol. 1 of *Eurocourses: Remote Sensing*, chap. Remote Sensing Systems: Sensors and Platforms, pp. 55–69.

[26] F. Vagni, "Survey of hyperspectral and multispectral imaging technologies," Tech. rep., The Research and Technology Organisation (2007).

[27] P. C. D. Hobbs, *Building Electro-Optical Systems: Making It all Work*, Wiley Series in Pure and Applied Optics (Wiley, 2000), 1st ed.

[28] J. M. Lerner, "Imaging spectrometer fundamentals for researchers in the biosciencesa tutorial," Cytometry Part A **69**, 712–734 (2006).

[29] D. J. Brady, *Optical imaging and spectroscopy* (Wiley Online Library, 2009).

[30] M. E. Gehm, M. S. Kim, C. Fernandez, and D. J. Brady, "High-throughput, multiplexed pushbroom hyperspectral microscopy," Opt. Express **16**, 11032–11043 (2008).

[31] D. L. Elmore, M.-W. Tsao, S. Frisk, D. B. Chase, and J. F. Rabolt, "Design and performance of a planar array infrared spectrograph that operates in the 3400 to 2000 cm-1 region," Appl. Spectrosc. **56**, 145–149 (2002).

[32] T. Kaneko, T. Namioka, and M. Seya, "Monk-gillieson monochromator," Appl. Opt. **10**, 367–381 (1971).

[33] I. L. Fujimori, C.-C. Wang, and C. G. Sodini, "A 256/spl times/256 cmos differential passive pixel imager with fpn reduction techniques," Solid-State Circuits, IEEE Journal of **35**, 2031–2037 (2000).

[34] Kodak, "Ccd image sensor. noise sources," Kodak Application Note pp. 585–722 (2005).

[35] H. Wach and E. R. Dowski, "Noise modeling for design and simulation of computational imaging systems," (2004), vol. 5438, pp. 159–170.

[36] J. Meola, M. T. Eismann, R. L. Moses, and J. N. Ash, "Modeling and estimation of signal-dependent noise in hyperspectral imagery," Appl. Opt. **50**, 3829–3846 (2011).

[37] M. Bouali and S. Ladjal, "Toward optimal destriping of modis data using a unidirectional variational model," Geoscience and Remote Sensing, IEEE Transactions on **49**, 2924 –2935 (2011).

[38] Z. Xiangjun, Y. Jianjun, S. Weidong, and C. Jinshu, "Stripe noise characteristic analysis and removal algorithms for hangtian tsinghua-1 satellite images," in "Info-tech and Info-net, 2001. Proceedings. ICII 2001 - Beijing. 2001 International Conferences on," , vol. 1 (2001), vol. 1, pp. 346–351.

[39] P. Meza, C. S. Martin, E. Vera, and S. Torres, "A quantitative evaluation of fixed-pattern noise reduction methods in imaging systems," in "Progress in Pattern Recognition, Image Analysis, Computer Vision, and Applications," , vol. 6419 of *Lecture Notes in Computer Science*, I. Bloch and J. Cesar, RobertoM., eds. (Springer Berlin Heidelberg, 2010), pp. 285–294.

[40] L.-R. Gao, B. Zhang, X. Zhang, W.-J. Zhang, and Q.-X. Tong, "A new operational method for estimating noise in hyperspectral images," IEEE Geoscience and Remote Sensing Letters **5**, 174–87 (2008).

[41] G. Corsini, M. Diani, and T. Walzel, "Striping removal in mos-b data," Geoscience and Remote Sensing, IEEE Transactions on **38**, 1439–1446 (2000).

[42] P. Meza, J. E. Pezoa, F. Parra, and S. N. Torres, "A prior knowledge model for multidimensional striping noise compensation in hyperspectral imaging devices," Proc. SPIE **8155**, 854222–854222–10 (2012).

[43] P. F. Inc., "Mv-d1024e series," `http://photonfocus.com/upload/flyers/flyer_A5_MV-D1024E_en_1.1.9.pdf` (2011).

[44] B. M. Ratliff, M. M. Hayat, and R. C. Hardie, "An algebraic algorithm for nonuniformity correction in focal-plane arrays," J. Opt. Soc. Am. A **19**, 1737–1747 (2002).

[45] U. Sakoglu, R. C. Hardie, M. M. Hayat, B. M. Ratliff, and J. S. Tyo, "An algebraic restoration method for estimating fixed-pattern noise in infrared imagery from a video sequence," (2004).

[46] S. E. Godoy, J. E. Pezoa, and S. N. Torres, "Noise-cancellation-based nonuniformity correction algorithm for infrared focal-plane arrays," Appl. Opt. **47**, 5394–5399 (2008).

[47] J. Zakrzewski and K. Didona, *Advancements in hyperspectral and multi-spectral imaging*. Available at `http://www.headwallphotonics.com/Portals/145999/docs/advancements%20in%20hyperspectral%20and%20multi-spectral%20ima.pdf`.

[48] *Advances in hyperspectral imaging technologies for multichannel fiber sensing*, vol. 7316.

[49] G. Shaw and D. Manolakis, "Signal processing for hyperspectral image exploitation," Signal Processing Magazine, IEEE **19**, 12–16 (2002).

[50] J. Zhang and G. Liu, "An efficient reordering prediction-based lossless compression algorithm for hyperspectral images," Geoscience and Remote Sensing Letters, IEEE **4**, 283–287 (2007).

[51] D. A. Scribner, K. A. Sarkady, M. Kruer, J. T. Caulfield, J. D. Hunt, and C. Herman, "Adaptive nonuniformity correction for infrared focal plane arrays using neural networks," Proc. SPIE **1541**, 100–109 (1991).

[52] A. Kumar, T. Radhika, V. Keerthi, D. Jain, V. Dadhwal, and A. Kumar, "Spectral deconvolution and non-overlap bands sampling for ims-1 hyperspectral imager data," Journal of the Indian Society of Remote Sensing pp. 1–6 (2013).

[53] A. Wong, "Adaptive bilateral filtering of image signals using local phase characteristics," Signal Processing **88**, 1615 – 1619 (2008).

[54] H. Peng and R. Rao, "Hyperspectral image enhancement with vector bilateral filtering," in "Image Processing (ICIP), 2009 16th IEEE International Conference on," (2009), pp. 3713–3716.

[55] A. Heo, J.-H. Lee, E.-J. Choi, W.-C. Choi, S. H. Kim, and D.-J. Park, "Noise reduction of hyperspectral images using a joint bilateral filter with fused images," (2011), vol. 8048, pp. 80481R–80481R–6.

[56] N. Acito, M. Diani, and G. Corsini, "Signal-dependent noise modeling and model parameter estimation in hyperspectral images," Geoscience and Remote Sensing, IEEE Transactions on **49**, 2957–2971 (2011).

[57] S. N. Torres and M. M. Hayat, "Kalman filtering for adaptive nonuniformity correction in infrared focal-plane arrays," J. Opt. Soc. Am. A **20**, 470–480 (2003).

[58] E. Vera and S. N. Torres, "Ghosting reduction in adaptive nonuniformity correction of infrared focal-plane array image sequences," in "Image Processing, 2003. ICIP 2003. Proceedings. 2003 International Conference on," , vol. 2 (2003), vol. 2, pp. II–1001–4 vol.3.